

1  
2  
3  
4  
5  
6  
7  
8  
9  
10  
11  
12  
13  
14  
15  
16  
17  
18  
19  
20  
21  
22  
23  
24  
25  
26

REVISE 2 – 15-06-2016

**Solid solution along the synthetic  $\text{LiAlSi}_2\text{O}_6$  (spodumene) –  $\text{LiFeSi}_2\text{O}_6$  (ferri-spodumene)**

**a general picture of solid solutions, bond lengths, lattice strains, steric effects,  
symmetries and chemical compositions of Li clinopyroxenes**

<sup>1,2,\*</sup>**Iezzi Gianluca**

<sup>3</sup>**Bromiley Geoffrey D.**

<sup>2,4</sup>**Cavallo Andrea**

<sup>5,6,7</sup>**Das Partha P.,**

<sup>5</sup>**Karavassili Fotini**

<sup>5</sup>**Margiolaki Irene**

<sup>8</sup>**Stewart Andrew A.**

<sup>9</sup>**Tribaudino Mario**

<sup>10</sup>**Wright Jonathan P.**

<sup>1</sup>Dipartimento di Ingegneria & Geologia, Università G. d'Annunzio, Chieti, Italy;

<sup>2</sup>INGV - Istituto Nazionale di Geofisica e Vulcanologia, Roma, Italy

<sup>3</sup>School of GeoSciences and Centre for Science at Extreme Conditions,

University of Edinburgh, Edinburgh, UK

<sup>4</sup>Laboratorio Tecnologico Multidisciplinare di Grosseto (CERTEMA),(GR), Italy and Istituto

Nazionale di Geofisica e Vulcanologia, Roma, Italy

<sup>5</sup>Department of Biology, University of Patras, Patras, Greece

<sup>6</sup>NanoMEGAS SPRL, Brussels, Belgium

<sup>7</sup>Electron Crystallography Solutions, Madrid, Spain

<sup>8</sup>Department of Physics and Energy, University of Limerick, Ireland

27 | <sup>9</sup> Dipartimento di Fisica e Scienze della Terra, Università di Parma, Italy

28 | <sup>10</sup>ESRF, 71 Avenue des Martyrs, 38000 Grenoble, France

29

30 | corresponding author: [gianluca.iezzi@unich.it](mailto:gianluca.iezzi@unich.it) (Iezzi Gianluca)

31

32 | **Running title:** LiAlSi<sub>2</sub>O<sub>6</sub> – LiFeSi<sub>2</sub>O<sub>6</sub> clinopyroxenes

33

34 | **Keywords:** lithium, clinopyroxenes, solid solutions, bond lengths, lattice strains, steric effects.

35

36

37

38

39

40

41

42

43

44

45

46

47

48

49

50

51

52

53

### Abstract

54 Seven clinopyroxene compositions along the join  $M^2Li^{M1}Al^T Si_2O_6$  (spodumene) to  
55  $M^2Li^{M1}Fe^{3+T} Si_2O_6$  (ferri-spodumene) were synthesized at 2 GPa, 800 °C under highly oxidizing  
56 conditions (using  $H_2O_2$  fluid) in an end-loaded piston cylinder. In addition, the  $LiFe^{3+} Si_2O_6$   
57 composition was also synthesized under the intrinsically reducing conditions in a piston cylinder, to  
58 check the effect of  $fO_2$  on iron speciation. The run-products were characterized by Field Emission  
59 Scanning Electron Microscope (FE-SEM), Rietveld refinements on XRPD synchrotron data and  
60 space group were assigned using SAED-TEM patterns. Run-products are composed mainly of  
61 lithium clinopyroxene (Li-cpx), plus minor amounts of hematite (magnetite under reducing  
62 condition) and corundum, as independently detected by image analysis (area %) and Rietveld  
63 refinements (wt. %); moreover, Rietveld results were used to derive cell parameters, M1-site  
64 occupancy (Al vs  $Fe^{3+}$ ), atomic positions and average bond lengths of all these Li-cpx indexed in  
65 the  $C2/c$  space groups according to SAED-TEM.

66 Li-cpx with Al and  $Fe^{3+}$  amounts close to 50:50 are actually slightly richer in Al a.p.f.u. than  
67 nominal; the  $LiFe^{3+} Si_2O_6$  grown under very oxidized and reducing conditions have very similar cell  
68 parameters, indicating that  $fO_2$  is unable to induce a significant incorporation of  $Fe^{2+}$  in these Li-  
69 cpx. The replacement of Al with  $Fe^{3+}$  induces a linear (%) increase of the cell edges following  $b > a$   
70  $> c$ , whereas  $\beta$  is roughly constant and the cell volume increases linearly. Furthermore, the  
71 substitution of Al with  $Fe^{3+}$  only weakly affects the T-O average length ( $< 1\%$ ), whereas M2-O and  
72 M1-O bonds increase linearly of 2.3 and 5.0 %, respectively.

73 These new experimental data have been compared with other available on Li-, Na and Ca-  
74 cpx, i.e.  $M^2(Li,Na,Ca,Mg,Fe^{2+})^{M1}(Mg,Fe^{2+}Al,Ni,Cr,Ga,V,Fe^{3+},Mn,Sc,In)^T Si_2O_6$ , to model lattice  
75 strain, bond lengths, steric effects and phase transitions behaviors. The replacement of Al with  
76 progressively larger cations in  $LiM^{3+} Si_2O_6$  cpx ( $M^{3+}$ : Ni, Cr, Ga, V,  $Fe^{3+}$ , Ti, Sc and In) results in a  
77 linear increase following  $V > b > a > c$ , whereas  $\beta$  is roughly constant except for Ti-end-member  
78 and  $P2_1/c$  compositions. Lattice strains induced by  $X$ ,  $T$  and  $P$  for Li-cpx in the  $C2/c$  stability field

79 show that when M1-site is progressively filled with a large cation,  $\epsilon_1$  axis ( $\epsilon_1 > \epsilon_2 > \epsilon_3$ ) increases  
80 along  $b$ , whereas  $\epsilon_2$  and  $\epsilon_3$  are nearly parallel to  $a$  and at about  $30^\circ$  from  $c$ . Conversely,  $T$  will  
81 provoke a similar enlargement of  $\epsilon_1$  and  $\epsilon_2$  along  $b$  and  $a$  edges, respectively, whereas  $\epsilon_3$  is again  
82 oriented at about  $30^\circ$  from  $c$ ; the increasing of  $P$  will instead shorten all strain tensor components  
83 ( $\epsilon_1$ ,  $\epsilon_2$  and  $\epsilon_3$ ) with a similar % amount; notably, high- $P$  is the only stress that induces a strain  
84 component to be almost parallel to  $c$  edge. Moreover, finite lattice strains and orientation in  $C2/c$   
85  $\text{LiMe}^{3+}\text{Si}_2\text{O}_6$  Li-cpx induced by  $\text{Me}^{3+}$ : Al- $\text{Fe}^{3+}$ ,  $\text{Fe}^{3+}$ -Sc, Sc-In are slightly different, with  $\epsilon_1$   
86 invariably lying along  $b$ ; conversely, Li-Na cation substitution is completely different with the  
87 highest and lowest deformations on the  $ac$  plane and  $\epsilon_2$  along  $b$ ;  $\epsilon_3$  vector is negative and oriented at  
88 about  $30^\circ$  from T-chains.

89 The ideal replacement of Al with larger cations up to In in Li-cpx induces the M1-O, M2-O  
90 and T-O average bond lengths to increase by 10.6, 4.3 and  $< 0.5\%$ . Steric effects in  $\text{Li}^{\text{M1}}\text{Me}^{3+}\text{Si}_2\text{O}_6$   
91 and  $\text{Na}^{\text{M1}}\text{Me}^{3+}\text{Si}_2\text{O}_6$  cpx are significant and very similar, whereas several other  $\text{Me}^{1+}$  and  $\text{Me}^{2+}$   
92 substitutions in cpx at both the M1 and M2-site, keeping fixed the other site, display less or even  
93 the absence of steric effects. Our new data also better elucidate relationships between Li-cpx  
94 composition, symmetry at room and non-ambient conditions and  $T_c$ . The aggregate cation radii at  
95 the M1-site does not exclusively control the stability of  $C2/c$  and  $P2_1/c$  polymorphs; instead valence  
96 electrons can profoundly favor the stabilization of a polymorph.

97 Finally, Li can be easily and accurately detected (0.1/0.2 a.p.f.u.) in natural clinopyroxenes  
98 by cell parameters, especially using the  $\beta$  angle.

99

100

101

102

103

104

105

## Introduction

106

107

108

109

110

111

112

113

114

115

116

117

118

119

120

Clinopyroxenes are widespread minerals with the crystal-chemical formula  $M1M2T_2O_6$  where most frequent cations at the M2-site are Na, Ca, Mg,  $Fe^{2+}$ , at M1-site are Mg,  $Fe^{2+}$ ,  $Fe^{3+}$ , Al and Ti, and where the T-site hosts prevalently Si and less commonly Al. In addition to these abundant compositions, Li-cpx can also be found in the late stage crystallization products of Si-rich magmas. The most common of these is the spodumene end-member  $^{M2}Li^{M1}Al^T Si_2O_6$  showing only limited cation substitutions towards  $^{M2}Na$ - and (more frequently)  $^{M1}Fe^{3+}$ -rich poles (Deer et al. 1997). Despite their very limited chemical variability and rarity in nature, Li-cpx have been extensively investigated in Earth and Material Sciences to derive the general crystal-chemical behavior of clinopyroxene as a function of chemical substitution (Ohashi et al. 2003; Kopnin et al. 2003; Redhammer and Roth 2004a; Nestola et al. 2008 and references therein), low- and high- $T$  thermal expansion and phase transitions (Tribaudino et al. 2003; Càmara et al. 2003; Redhammer and Roth 2004b; Tribaudino et al. 2009; Redhammer et al. 2010 and references therein), high- $P$  (Artl and Angel 2000; Gatta et al. 2005; Pommier et al. 2005; Nestola et al. 2008, 2009; Periotto et al. 2013 and references therein), as well as magnetic properties (Redhammer et al. 2001, 2010; Zhou et al. 2014).

121

122

123

124

125

126

127

128

129

130

All these studies have greatly improved our general understanding of physical and chemical properties at ambient and non-ambient conditions and the phase transition behavior of single-chain silicates (and analogue-germanates); the complex puzzle of crystal-chemistry and phase transitions of Li-cpx provides a model for the generalized description of the response of structure to  $X$ ,  $T$  and  $P$  in chain silicates and in silicates in general. However, substitution of Al with  $Fe^{3+}$  at M1-site for Li-cpx remains to be investigated. To fill this gap, we prepared seven compositions along this nominal join, i.e. from spodumene ( $LiAlSi_2O_6$ ) to ferri-spodumene ( $LiFe^{3+}Si_2O_6$ ). Experiments were performed at high- $T$ , - $P$  and extremely high  $fO_2$  conditions; we also synthesized another nominal ferri-spodumene composition but at moderate (intrinsic)  $fO_2$  to induce a possible incorporation of significant amount of  $Fe^{2+}$ . We characterized these eight run-products by both scanning (FE-SEM)

131 and transmission (TEM) electron microscopes, in addition to synchrotron X-ray powder diffraction  
132 (XRPD) to quantitative constrain yield, composition and the symmetry of crystalline phases.

133 Our experimental results allow us to further depict: i) the general crystal-chemical behavior  
134 of  $\text{LiMe}^{3+}\text{Si}_2\text{O}_6$  clinopyroxenes ( $\text{Me}^{3+} = \text{Al to In}$ ), ii) the comparison of lattice deformations  
135 induced by chemical substitution at the M1-site *vs* those induced by *T* and *P* for Li-cpx, steric  
136 effects induced by cations at M1- and M2-site in clinopyroxenes and iii) the parameters that impose  
137 at ambient conditions the *C2/c* symmetry of these compounds. In fact it appears that the cation  
138 radius of the cation substituting in the M1 site is not sufficient to account for the symmetry of the  
139 studied phases.  $\text{Li}(\text{Al,Fe}^{3+})\text{Si}_2\text{O}_6$  clinopyroxenes have an M1-site cation size higher than 0.535 and  
140 lower than 0.645 Å, whereas in the same cation range  $\text{LiNiSi}_2\text{O}_6$  and  $\text{LiCrSi}_2\text{O}_6$  display *P2<sub>1</sub>/c*  
141 symmetry and cation radius 0.560 (in low spin state) and 0.615 Å, respectively. This contribution is  
142 a further piece of knowledge in the complex puzzle of crystal-chemistry of Li-cpx; the general  
143 outcomes and conclusions attained here can be extended to the entire clinopyroxene, and possibly to  
144 all chain-silicates.

145

146

### Experimental methods

147 *Starting materials and sample charges.* The two end-member  $\text{LiAlSi}_2\text{O}_6$  and  $\text{LiFe}^{3+}\text{Si}_2\text{O}_6$   
148 compositions were prepared by mixing for 2 hours in an automatic mortar  $\text{Li}_2\text{SiO}_3 + \text{Al}_2\text{O}_3 + \text{SiO}_2$   
149 and  $\text{Li}_2\text{SiO}_3 + \text{Fe}_2\text{O}_3 + \text{SiO}_2$  high-purity reagents, in stoichiometric amounts (1:1:3). The two fine-  
150 grained powders were mixed to prepare the five intermediate compositions (Table 1).  
151 Approximately 70 mg of each starting composition were loaded in AgPd capsules with a length of 5  
152 mm; we also added 10 wt.% of  $\text{H}_2\text{O}_2$  (with  $\text{O}_2 \sim 30$  wt.%) to each starting composition to prevent  
153 the reduction of  $\text{Fe}^{3+}$  to  $\text{Fe}^{2+}$  (Tab. 1), since the intrinsic redox state in piston cylinder experiments  
154 is reducing due to pressure media and furnace materials (Iezzi et al. 2003a, 2003b, 2005; Della  
155 Ventura et al. 2005). To check this experimental strategy, we prepared a capsule with  $\text{LiFe}^{3+}\text{Si}_2\text{O}_6$   
156 starting material plus 10 wt.% of  $\text{H}_2\text{O}$ , to compare  $\text{LiFe}^{3+}\text{Si}_2\text{O}_6$  run-products synthesized in  $\text{H}_2\text{O}_2$ -

157 bearing with H<sub>2</sub>O<sub>2</sub>-free charges (Table 1). The capsules were carefully weighed before and after  
158 welding in order to check loss of weight that would indicate the loss of O<sub>2</sub> and/or H<sub>2</sub>O<sub>2</sub>.

159 *High-T and -P experiments.* Two capsules per experiment were then inserted in dry alumina  
160 cylinder sleeves; these capsule holders were then inserted in cylinders of graphite used as furnace to  
161 generate high temperature. Finally, these assemblage of graphite were placed in dry salt-pyrex  
162 (pressure medium) piston-cylinder assemblages. All experiments were carried out at 2 GPa and at  
163 800 °C using the “hot piston in” method in an end-loaded piston cylinder apparatus installed at the  
164 Bayerisches Geoinstitut using a 0.5 inch internal diameter bomb (Iezzi et al. 2005). The  
165 temperature was monitored with an accuracy of ± 10°C using a Pt–Pt<sub>90</sub>Rh<sub>10</sub> thermocouple placed  
166 close to the sample charges and separated from it (about 2 mm) with an alumina disk. Pressure was  
167 calibrated against the quartz–coesite and kyanite–sillimanite transitions, as well as the melting point  
168 of diopside, and is estimated to be accurate to within ± 5% of the stated value (as described fully in  
169 Bromiley et al. 2004). Each experiment lasted about 3 days; then, isobaric quenching was achieved  
170 by switching off the power supply, with a decreasing in *T* from 800 °C down to 500 °C invariably  
171 over less than 10 s.

172

173

### **Analytical methods**

174 *FE-SEM and image analysis.* Images and chemical data were collected at the micron scale  
175 by FE-SEM Jeol-JSM6500F (FESEM) installed at the INGV of Roma. The size, shape, distribution,  
176 type and abundance of the synthesized phases, i.e. textures (Higgins 2006), were investigated using  
177 electron microscopy back scattered images acquired on polished run-products mounted in epoxy  
178 resin in a range of magnifications from 150X to 1500X to highlight general and detailed textural  
179 features per sample, respectively. For each run-product we selected two FE-SEM fields of view to  
180 quantify the phase abundance by image analysis. The image analysis protocol was the same  
181 frequently used in petrological studies (Higgins 2006; Iezzi et al. 2008, 2011; Lanzafame et al. 2013  
182 and references therein). For each phase a range of grey-levels was determined which scaled with

183 average chemical composition. Then, we automatically counted the area% of these phases with  
184 Image-ProPlus 6.0 software, avoiding any mathematical correction of these data (Iezzi et al. 2008,  
185 2011a; Lanzafame et al. 2013; Vetere et al. 2013, 2015). The presence of Li in the phase  
186 assemblages as well as the relative slight zonation of Li-cpx containing both Al and Fe (possibly  
187 Fe<sup>2+</sup> and Fe<sup>3+</sup>) limit the accuracy of micro-chemical data collected by Energy Dispersive  
188 Spectroscopy during the FESEM observations. Hence, we checked the amount of Fe vs Al by  
189 Rietveld refinement (see below) and using crystal-chemical constraints.

190 *SAED-TEM*: We collected a series of electron diffraction patterns from the eight run-  
191 products. Initially, all samples were prepared by crushing the raw material with a mortar and pestle  
192 to a fine powder and dispersing each sample on a 200 mesh Copper TEM grid with a continuous  
193 film of amorphous carbon. The diffraction patterns were collected at an accelerating voltage of 200  
194 keV using a JEOL 2100 transmission electron microscope with a LaB<sub>6</sub> filament, available at the  
195 department of Biology, at University of Patras, Greece. The data were collected in selected area  
196 diffraction (SAD) mode, using a parallel beam and a 70 μm C2 aperture and were recorded from a  
197 Gatan ES500W, a 12-bit charge-coupled device (CCD). Selected area diffraction patterns were  
198 obtained by selected sub-region of the crystal using a 50 μm diameter SAD aperture. Crystals of  
199 approximately 400 nm were located in imaging mode; the diffraction data were then collected  
200 following the manual diffraction tomography (MDT) method (Gorelik et al. 2011), by rotating the  
201 crystal around an arbitrary axis and diffraction patterns were collected every 1° of tilt. A standard  
202 single tilt JEOL holder permitted us a tilting of ± 30°. At each step, a static diffraction pattern and  
203 then a precessed diffraction pattern was collected using the spinning star precession unit  
204 (Nanomegas SPRL: <http://www.nanomegas.com>, Belgium).

205 Tilting a crystal around an arbitrary crystallographic axis reduces the dynamical diffraction  
206 effects, inevitable in electron diffraction and the data are treated as being kinematical. The reduction  
207 in dynamical scattering occurs because fewer reflections are excited simultaneously, thus less  
208 dynamical scattering is detected and the intensities recorded are more reliable. The use of



209 precession in this experimental setup is to integrate the reciprocal volume. A precession semi-angle  
210 of 1° was used to integrate the data, meaning a 2° volume was integrated, and there is overlap  
211 between each diffraction pattern. The purpose of this is to allow us only to consider fully integrated  
212 reflections during the data processing steps. Partially integrated reflections are disregarded,  
213 significantly reducing the complexities of the data analysis.

214 Cross-validation of the data was performed by collecting additional data on one sample of  
215 this series (Fe#0) at the Institute of Physical Chemistry, in Mainz, using an FEI TECNAI F30  
216 transmission electron microscope, operating at 300 keV. Diffraction patterns, in this case, were  
217 collected using a defocused stem probe, which is a quasi-parallel beam made by using a 10 µm C2  
218 aperture and a large defocus. The patterns were recorded from a 14 bit Gatan 794MSC slow scan  
219 CCD detector. Data obtained from both instruments were of comparable quality, enabling us to  
220 define assuredly the space group symmetry. Experimental diffraction patterns, from each sample,  
221 were processed using the ADT3D software (NanoMEGAS SPRL, Belgium).

222 *Synchrotron XRPD.* A monochromatic X-ray beam ( $\lambda = 0.3263 \text{ \AA}$ ) at the ID11 beamline of  
223 the ESRF in Grenoble (France) was used for collecting data on a 2D area detector (Frelon 2K CCD)  
224 (Labiche et al. 2007) with a 2048 x 2048 pixel resolution and pixel size  $\sim 47 \times 47 \text{ \mu m}$ . The beam  
225 centre was offset on the 2D detector to give improved angular resolution. The sample to detector  
226 distance was calibrated using CeO<sub>2</sub> powder at 186.6 mm. Samples were mounted for diffraction  
227 measurements by picking up a small fragment from the powder sample using a cryoloop and  
228 paratone oil. Data collection was performed by rotating the samples over a range of 360° in steps of  
229 20° giving 18 images in total per sample. This rotation scan was repeated with two different X-ray  
230 beam sizes; 0.05 x 0.05 and 0.3 x 0.3 mm. With the small beam size the powder data have sharper  
231 peaks but the powder averaging is not as good compared to the data set from the large beam size  
232 and lower angular resolution. Images from the rotation scan were averaged and integrated using the  
233 fit2d software package (Hammersley et al. 1996).

234 Based on SEM data, we assigned peaks in diffraction patterns to the crystalline phases grown  
235 in each run-product. Then, all the diffraction patterns were first refined with the software EXPGUI-  
236 GSAS (Larson and Von Dreele 1997; Toby 2001) using the Le Bail method (Le Bail 2005),  
237 following the procedure adopted by Iezzi et al. (2010) and (2011b) to accurately model background  
238 (Chebyshev function with 10-12 adjustable parameters), cell parameters (of all crystalline material)  
239 and pseudo-Voigt peak shape function (Finger et al. 1994). After that the Le Bail models fully  
240 reproduced each recorded XRPD patterns, we fixed these parameters (background, cell and profile  
241 of Bragg peaks) and determined with Rietveld refinement the phase abundance (wt. %), atomic  
242 positions using isotropic displacement parameters per crystallographic site and cation occupancy at  
243 the M1-site. For all the run-products with Al and Fe (Tables 1 and 2) we fixed the amount of Li and  
244 Si both at 1 and 2 a.p.f.u. at M2- and T-sites, respectively, whereas the amount of Al vs Fe<sup>3+</sup> were  
245 refined using the constraint that their sum is 1 a.p.f.u. In contrast, the Fe<sup>2+</sup> run-product was not  
246 refined with Rietveld approach, since it was not possible to attain a satisfactory determination of Li  
247 vs Fe<sup>2+</sup> at the M2-site and especially Fe<sup>2+</sup> vs Fe<sup>3+</sup> at the M1-site.

248 For each run-product, at the beginning of Le Bail and Rietveld refinements we used the  
249 crystal structural models of spodumene and ferri-spodumene reported in Redhammer and Roth  
250 (2004a) for the most Fe-poor (LiAlSi<sub>2</sub>O<sub>6</sub>) and Fe-rich (LiFe<sup>3+</sup>Si<sub>2</sub>O<sub>6</sub>) run-products, respectively, plus  
251 the starting models of corundum and hematite from the ICSD (Inorganic Crystal Structural  
252 Database). According to TEM data (see below), we refined all clinopyroxene in the *C2/c* space  
253 group; at the end of each Rietveld refinement a good reproduction of experimental XRPD patterns  
254 were attained, agreement indexes were of high quality and un-indexed Bragg reflections were not  
255 recognized (Table 2). We further validated our Rietveld refinement by comparing cell parameters  
256 and bond lengths measured here for the two end-members with those obtained by single crystal X-  
257 ray diffraction (SC-XRD) for LiAlSi<sub>2</sub>O<sub>6</sub> and LiFe<sup>3+</sup>Si<sub>2</sub>O<sub>6</sub>, as reported by Redhammer and Roth  
258 (2004a).

259

260

## Results

261 | *Textures of Li-cpx.* The textural features of the run products are displayed in Fig. 1. The  
262 area% of phases quantified by image analysis is reported in Table 3. Clinopyroxene is by far the  
263 most abundant phase in any sample. Minor amounts of corundum plus tiny and rare crystals of an  
264  $\text{Al}_2\text{SiO}_5$  phase, probably kyanite, occur in the Fe#0 and Fe#20 run-products (Figs. 1 and 2).  
265 Hematite is present in the other Fe-bearing run-products synthesized with  $\text{H}_2\text{O}_2$  (Fe#20, Fe#40,  
266 Fe#50, Fe#60 Fe#80 and Fe#100 run-products); the Fe#2+ run-product is composed of Li-cpx and  
267 few tiny crystals of magnetite (Figs. 1 and 2).

268 Non-crystalline materials have been not detected by FE-SEM, probably due to their low  
269 amount in area% (and/or wt.%). Small amounts of corundum and of an  $\text{Al}_2\text{SiO}_5$  phase, hematite and  
270 magnetite in the Fe#0, Fe#100 and Fe#2+ experimental charges, respectively (Table 3), indicates  
271 the presence of a very low amount of a phase (or phases) composed of Li, Si and O, possibly the  
272 non-crystalline  $\text{Li}_2\text{SiO}_3$  phase solidified during quenching. Li-cpx with intermediate amount of Al  
273 and Fe of this study show slight chemical zoning, especially the Fe#40 and Fe#50 samples (Fig. 1).  
274 Quantitatively, the amount of un-desired phases of corundum, hematite plus magnetite is lower than  
275 ~ 10 area% in any experimental charge, and lower in the end members; in turn, the yield of Li-cpx  
276 is always higher than 90 area% (Figs. 1 and 2 and Table 3). The stoichiometry of these Li-cpx was  
277 not analyzed directly by micro-chemical data, although the low amount of the other un-desired  
278 phases with simple chemistries (corundum, hematite and magnetite), suggest that the departure of  
279 all synthesized Li-cpx from the nominal composition is limited. Under an extremely oxidizing  
280 environment, i.e.  $\text{Fe}^{2+}$ -free, and with Li-cpx amount higher than 90 area% (and wt.% except for the  
281 Fe#40 and Fe#50) (Table 3), the chemical variations of these Li-cpx is restricted to the M1 site; in  
282 turn, their chemical compositions can be straightforwardly calculated by XRPD data by refining  
283  $\text{Al}_x\text{Fe}^{3+}_{1-x}$ , where  $0 \leq x \leq 1$  (see below).

284 The shape of Li-cpx is invariably nearly equant with crystal lengths equal or double their  
285 widths, i.e. aspect ratio range from 1 to 2. By contrast, the absolute size strongly increases with Fe

286 content (Fig. 1). The three Al richer run-products have maximum crystal size dimension invariably  
287 lower than 10  $\mu\text{m}$ , up to 15-20  $\mu\text{m}$  for the Fe#50 and Fe#60 samples, around 20-25  $\mu\text{m}$  for the  
288 Fe#80 crystals, whereas Fe#100 and Fe#2+ show crystal maximum edges up to about 100 and 200  
289  $\mu\text{m}$ , respectively (Fig. 1).

290 *Space group of Li-cpx.* Data analysis of diffraction tomography patterns, using a preprocessed  
291 beam, allowed for space group determination due to the reduced dynamical scattering and multiple  
292 diffraction. All single crystals employed exhibit similar monoclinic symmetry. Accurate unit cell  
293 parameters however were extracted without precessing the beam, because later adds a significant  
294 error to the positions of the reflections. For this reason we used the diffraction patterns from a  
295 stationary beam to determine a more accurate unit cell size (Table 4)

296 The reciprocal volumes were reconstructed from the measured intensities, and the volume  
297 was checked for systematic absences. From the observed extinction conditions, the space groups  
298  $C2/c$  and  $Cc$  were selected, both were tested, and  $C2/c$  was derived as the most feasible solution  
299 (Table 3). The 3D reconstruction of the reciprocal space from the extracted intensities, for one  
300 representative run product, Fe#50, presented in Fig. 3 shows the violation of extinction conditions  
301 for all other possible monoclinic space groups. The output from ADT3D software is a list of  
302 reflections with their Miller indices and intensities. Additionally, processing the extracted  
303 reflections, using the direct methods software SIR2014 (Burla et al. 2015), also confirmed  $C2/c$  and  
304  $Cc$  as the most likely space groups, with the highest figures of merit.

305 *Cell parameters, site occupancy and bond lengths of Li-cpx from XRPD.* The agreement  
306 indexes of Rietveld refinements for all run-product crystallized with  $\text{H}_2\text{O}_2$  fluid are lower than 5 %  
307 (except  $R_p$  for Fe#100) (Table 2). As Fe content increases the diffraction peaks of Li-cpx become  
308 broader (Fig. 1) and their diffraction patterns show also an increase of “spottiness” (Fig. 4) (Debye  
309 rings are lesser and lesser continuous) roughly from Fe#0 to Fe#100 due to sample preparation. In  
310 turn, a progressive reduction in accuracy of crystallographic results are observed for the Fe#100 Li-  
311 cpx due to a slight increasing of crystallographic preferred orientation of Li-cpx crystallites (Fig. 4

312 and Tab 2). Even with these minor limitations, the calculated Rietveld patterns accurately  
313 reproduced the experimental XRPD pattern (Fig. 4S).

314 The amount of crystalline phases in wt.% and the site occupancies at the M1-site, i.e. the  
315 actual crystal-chemical formula of Fe#20 to Fe#80 Li-cpx, are reported in Table 3. The actual and  
316 nominal comparison of our Li-cpx are displayed again in Fig. 2, as well as the amount of crystalline  
317 phases determined by Rietveld (wt. %) vs image analysis (area %). The majority of our Li-cpx show  
318 a very slight deviation from the nominal composition, except for the run-products Fe#40 and Fe#50  
319 that are richer in Al and poorer in Fe<sup>3+</sup> compared to their nominal compositions, in agreement with  
320 the presence of hematite (Fig. 2 and Table 3). The discrepancy between area% and wt.% phase  
321 proportions per each run-product is very small, with maximum differences for the Fe#40 and Fe#60  
322 samples (Fig. 2). Taking into account that the actual composition of Fe#60 Li-cpx is close to the  
323 nominal one, it could be inferred that Fe#60 Li-cpx has an actual composition richer in Al a.p.f.u.  
324 than measured by Rietveld refinement (Tables 3 and 5, Fig. 2). For the Fe#2+ run-product a direct  
325 determination of site occupancies was not attainable, due to the possible presence of Fe<sup>2+</sup> at both  
326 M1- and M2 site for local charge balance requirements (Cámara et al. 2003, 2006); however, its  
327 composition can be constrained by cell parameter data (see below).

328 The evolution of *a*, *b*, *c*,  $\beta$  cell and volume parameters are reported in Table 4 and displayed  
329 in Fig. 5. The cell data refined here on polycrystalline Li-cpx with LiAlSi<sub>2</sub>O<sub>6</sub> (Fe#0) and  
330 | LiFe<sup>3+</sup>Si<sub>2</sub>O<sub>6</sub> (Fe#100) compositions are practically identical to those obtained by single crystal data  
331 (Redhammer and Roth 2004a, 2004b). All our cell parameters determined here can be thus  
332 considered highly accurate, as well as the crystal-chemistry of our Li-cpx end-members, i.e.  
333 absence of any Fe<sup>2+</sup> at both M1- and M2-sites. Therefore, all Li-cpx grown with H<sub>2</sub>O<sub>2</sub> have only Li  
334 and Si at M2- and T-site, respectively, whereas M2 site is occupied only by Al and Fe<sup>3+</sup>; the  
335 absence of Fe<sup>2+</sup> agrees with the crystallization of hematite (Table 3).

336 The replacement of Al with Fe<sup>3+</sup> induces a linear (%) increase of the cell edges following *b*  
337 > *a* > *c*, whereas  $\beta$  is roughly constant (Fig. 5); the cell volume increases linearly by about 6 %

338 from spodumene to ferri-spodumene. The Fe<sup>#2+</sup> Li-cpx grown at reducing intrinsic  $fO_2$  shows a  
339 very limited deviation of its cell data in comparison to Li-cpx in Fe#100 and to that determined in  
340 Redhammer and Roth (2004a). This suggests that although the redox state is markedly different  
341 between the Fe<sup>#2+</sup> and Fe#100 syntheses, i.e. reducing intrinsic vs H<sub>2</sub>O<sub>2</sub> experimental conditions  
342 and reflected by the crystallization of hematite and magnetite, respectively, Li-cpx is unable to  
343 incorporate a significant amount of Fe<sup>2+</sup> at both M1- and M2-sites, as it would be required by  
344 charge balancing (Càmara et al. 2003, 2006). Moreover, the Fe#100 and Fe<sup>#2+</sup> run-products have  
345 dark red and green colors, respectively. This suggests that Li-cpx in Fe<sup>#2+</sup> contains some Fe<sup>2+</sup>  
346 amounts; however, due to the high similarities in cell parameters (Fig. 5), it can be expected that the  
347 amount of Fe<sup>2+</sup> which can be incorporated is limited. As an evidence, the  $\beta$  angle of Li-cpx is  
348 extremely sensitive to cation occupancy at M2-site; Fe<sup>#2+</sup> and Fe#100 have practically the same  $\beta$   
349 of 110.2° (Table 4), whereas the (Li<sub>0.85</sub>Mg<sub>0.09</sub>Fe<sup>2+</sup><sub>0.06</sub>)(Fe<sup>3+</sup><sub>0.85</sub>Mg<sub>0.15</sub>)Si<sub>2</sub>O<sub>6</sub> cpx has 109.83° (Càmara  
350 et al. 2003). To summarize, Li-cpx in Fe<sup>#2+</sup> has a crystal-chemical formula lying along (Li<sub>1-x</sub>  
351 Fe<sup>2+</sup><sub>x</sub>)(Fe<sup>2+</sup><sub>x</sub>Fe<sup>3+</sup><sub>1-x</sub>)Si<sub>2</sub>O<sub>6</sub> with x (0 ≤ x ≤ 1) close to 0 a.p.f.u.. The amount of Fe<sup>3+</sup> is instead well  
352 constrained by Rietveld refinement for all other Fe-bearing Li-cpx, due to the significant difference  
353 in scattering of X-ray by Al vs Fe. The slight horizontal offsets of Fe#60 and Fe#80 Li-cpxs in Fig.  
354 5 from the linear regressions can be due to a slight underestimation of Al; nonetheless, this  
355 discrepancy is invariably below 0.05 a.p.f.u (Fig. 5).

356 The atomic positions and derived average bond lengths are reported in Tables 5 and 6 and  
357 plotted in Fig. 6. Again, these data are compared with single crystal X-ray structural refinement for  
358 LiAlSi<sub>2</sub>O<sub>6</sub> and LiFe<sup>3+</sup>Si<sub>2</sub>O<sub>6</sub> (Redhammer and Roth 2004a, 2004b). These average bond lengths are  
359 almost identical to those refined here by XRPD for Fe#0 and Fe#100, respectively (Fig. 6).  
360 Substitution of Al with Fe<sup>3+</sup> only weakly affects the T-O average length (< 1 %). Instead M2-O and  
361 M1-O bonds both increase by 2.3 and 5.0 % (Fig. 6). Similarly to cell parameters, also M2- and  
362 M1-O average bond lengths evolve in a linear manner.

363

364

## Discussion

365 *Li-cpx cell parameters.* The investigated spodumene - ferri-spodumene join is the first  
366 substitution vector involving a metal and a non-metal cations at M1-site of Li-cpx. Here, the XRPD  
367 and TEM data point out that Al can be completely replaced by Fe<sup>3+</sup> (at 800 °C and 2 GPa), the solid  
368 solution is nearly ideal due to an almost linear evolution of cell volume and space group is  
369 invariably *C2/c* at room conditions (Figs. 3, 5 and 6, Tables 2, 3, 4, 5 and 6). As mentioned  
370 previously, these new data allow further clarification of several general crystal-chemical features of  
371 Li-cpx, that are one of the most detailed investigated silicate sub-groups (room-*T* and -*P*, low- and  
372 high-*T*, high-*P*). Therefore, it is possible to model relations between structural and compositional  
373 parameters using previous data on Li-cpx with those provided here. The general constraints of Li-  
374 cpx can be then extrapolated to the entire clinopyroxene family or even for the chain silicates super-  
375 group.

376 The first important outcome concerns the evolution of cell parameters of LiMe<sup>3+</sup>Si<sub>2</sub>O<sub>6</sub>, with  
377 <sup>VI</sup>Me<sup>3+</sup> ranging from Al to In, corresponding to an increase in cation radii from 0.535 to 0.800 Å,  
378 respectively. This substitution is only theoretical, since a direct exchange of the smallest with the  
379 largest <sup>VI</sup>Me<sup>3+</sup> cation is not yet proved and probably is limited due to the significant difference in  
380 atom size dimension of about 33 % [ $\Delta\% = (r^{\text{In}} - r^{\text{Al}}) / r^{\text{In}}$ ]. The evolution of cell volume at ambient  
381 conditions for Li-cpx as a function of the M1-site occupancy, with M2- and T-site occupied only by  
382 Li (except the sample of Càmara et al. 2003) and Si, respectively, is displayed in Fig. 7. This  
383 increasing trend as a function of Me<sup>3+</sup> cation size is almost linear, with only a slight tendency to  
384 level off from Sc to In. The Li-cpx for whom temperatures of displacive phase transitions (*T*<sub>c</sub>) are  
385 determined are also reported (Fig. 7). *P2<sub>1</sub>/c* Li-cpx structural polymorphs have two not-  
386 symmetrically equivalent tetrahedral chains, one kinked and one relatively extended as classically  
387 measured by the O3-O3-O3 angle, whereas *C2/c* polymorphs have equivalent and extended  
388 tetrahedral chains. Large M1 cation and high-*T* tend to stabilize the *C2/c* structural topology (Arlt  
389 and Angel 2000; Tribaudino et al. 2009). A third polymorph has again the *C2/c* space group but

390 with strongly kinked equivalent T-chains and is stabilized at high-*P* (Arlt et al. 1998; Arlt and  
391 Angel 2000). Compared to *C2/c*, *P2<sub>1</sub>/c* Li-cpx at room show only a very minor cell volume  
392 deviation with respect to the linear regression (Fig. 7); LiNiSi<sub>2</sub>O<sub>6</sub>, invariably *P2<sub>1</sub>/c* at least up to 773  
393 K (Tribaudino et al. 2009), most offsets down the linear regression (Fig. 7). On the other hand, *C2/c*  
394 LiTiSi<sub>2</sub>O<sub>6</sub> most offsets upwards the linear regression (Fig. 7).

395 The same cell edge trends as a function of the M1 cation radii are reported in Fig. 7S; as are  
396 the *a*, *b* and *c* edges which also increase as the M1-site size augments, similar to cell volume  
397 evolution. However, the *a* cell edge increases only from Al to Sc; further cation substitution,  
398 between Sc and In, does not promote an increase in the *a* cell parameter. *P2<sub>1</sub>/c* Li-cpx at room  
399 temperature/pressure are almost indistinguishable by their *b* and *c* cell edges, whereas the *a*  
400 parameter is slightly downshifted respect to the general trend (Fig. 7S). A larger downshift is found  
401 for the LiNiSi<sub>2</sub>O<sub>6</sub> clinopyroxene. With the exception of the LiTiSi<sub>2</sub>O<sub>6</sub> compound, the three Li-cpx  
402 with a *P2<sub>1</sub>/c* space group at ambient conditions are clearly off trend for the monoclinic  $\beta$  angle (Fig.  
403 7S). Resuming, Li-cpx with variable cation at the M1-site and thus size at room-*T* and -*P* have *b*  
404 and *c* cell edges that increase linearly and Li-cpx with *P2<sub>1</sub>/c* and *C2/c* space groups are  
405 indistinguishable. By contrast, *a* cell first increases in a linear way and then saturates from Sc to In;  
406 *a* and especially the monoclinic  $\beta$  angle promptly discriminates *P*- to *C*-lattice, except for the  
407 LiTiSi<sub>2</sub>O<sub>6</sub> pole (Figs 7S). Finally, the  $a \sin \beta$  dimension, corresponding to the distance between  
408 parallel T-chains, follow the same trend of the *a* cell alone (Figs. 7S).

409 *Li-cpx cell strains.* We calculate the strain tensor induced by cell parameter variations, using  
410 the program “win\_strain” compiled by R.J. Angel ([http://www.rossangel.com/text\\_strain.htm](http://www.rossangel.com/text_strain.htm)).  
411 Thus, we calculate lattice strains using selected couples of cell parameters plotted in Fig. 7S of  
412 LiMe<sup>3+</sup>Si<sub>2</sub>O<sub>6</sub>, where Me<sup>3+</sup> > Al up to In, always with respect to that of LiAlSi<sub>2</sub>O<sub>6</sub>. Hence, from the  
413 smallest cation Al at M1-site towards In, we outlined lattice strain paths by calculating the  
414 orthogonal finite strain tensor (%)  $\epsilon_1$ ,  $\epsilon_2$  and  $\epsilon_3$  components ( $\epsilon_1 > \epsilon_2 > \epsilon_3$ ) and their orientations with  
415 respect to Li-cpx cell. Monoclinic symmetry imposes a strain vector that is fixed along *b*, whereas



416 the other two components are on the 010 plane and form an angle with  $a$  and  $c$  edges (Gatta et al.  
417 2005; Iezzi et al. 2005, 2010, 2011b and reference therein). The lattice deformation of Li-cpx  
418 induced by chemical substitution (X) at M1-site is displayed in Fig. 10 and compared with those  
419 induced by  $T$  and  $P$  for  $\text{LiAlSi}_2\text{O}_6$  and  $\text{LiFe}^{3+}\text{Si}_2\text{O}_6$  end-members in the  $C2/c$  stability fields. We  
420 also reported a structural model of Li-cpx plotted down  $b$  edge, to facilitate the visualization of the  
421 deformations as a function of the structure of Li-cpx.

422 The substitution of Al with larger cations at M1 induces that the highest deformation, i.e.  $\varepsilon_1$ ,  
423 is along  $b$ , whereas  $\varepsilon_2$  and  $\varepsilon_3$  are disposed at about 15/20 and 105/110 ° from  $c$  on the 010 surface up  
424 to Sc then they suddenly re-orient to 35 and 125 ° from  $c$  when Li-cpx approach the In pole (Fig. 8).  
425 The deformations induced by the substitutions of Al with Ni and Cr from a C- to P-lattices (to be  
426 directly investigated) occur under a slightly different orientation for Ni and very similar to other C-  
427 lattice for Cr. The still undetermined phase transition occurring between Al and Ni again has  $\varepsilon_1$   
428 fixed along  $b$ , but  $\varepsilon_2$  and  $\varepsilon_3$  are disposed along and normal to  $c$ , respectively, very differently from  
429 all other lattice strains induced by chemical substitution; moreover, the  $\varepsilon_3$  component is negative,  
430 hence the replacement of Al by Ni should be accompanied by an expansion of Li-cpx along  $b$  and  $c$   
431 and a contraction along  $a$  (Fig. 8). The % variation of finite strain components induced by the  
432 increasing size of M1 cation radii is similar for  $\varepsilon_2$  and  $\varepsilon_3$ , whereas  $\varepsilon_1$  has a significantly higher  
433 increasing rate towards the In end-member (Fig. 8). Specifically,  $\varepsilon_2$  first increases and then levels  
434 off, whereas  $\varepsilon_3$  has invariably the same trend with a very low rate of increase (Fig. 8). On the whole,  
435 the increasing size of cation radii at M1-site imposes the highest deformation ( $\varepsilon_1$ ) along  $b$ , and a  
436 moderate to low strain on the other two mutual orthogonal components ( $\varepsilon_2$  and  $\varepsilon_3$ ) on the  $ac$  plane  
437 (Fig. 8). The virtual substitutions of Al with Ga, V,  $\text{Fe}^{3+}$ , Ti, Sc and In result in normalized strain  
438 components ( $\varepsilon_1/\varepsilon_1:\varepsilon_2/\varepsilon_1:\varepsilon_3/\varepsilon_1$ ) of 1:0.60:0.52, 1:0.75:0.47, 1:0.67:0.43, 1:0.64:0.44, 1:0.55:0.38 and  
439 1:0.48:0.37, respectively; indeed, the  $\varepsilon_1$  component increases more than  $\varepsilon_2$  and  $\varepsilon_3$  moving from Al to  
440 In (Fig. 8).

441 To compare lattice deformations induced by chemical substitution with those induced by  
442 temperature and pressure it has been considered only the two  $\text{LiAlSi}_2\text{O}_6$  and  $\text{LiFe}^{3+}\text{Si}_2\text{O}_6$  poles with  
443 the  $C2/c$  space group (with tetrahedral chains extended). From room temperature to around 700 °C,  
444 lattice deformations of both  $\text{LiAlSi}_2\text{O}_6$  and  $\text{LiFeSi}_2\text{O}_6$  poles are similar in orientation and  
445 magnitude. The  $\epsilon_1$  and  $\epsilon_2$  are very close between them although their deformation accounts less than  
446 1%. The highest strain  $\epsilon_1$  component is along  $b$  and at about 120 ° from  $c$  for  $\text{LiAlSi}_2\text{O}_6$  and  
447  $\text{LiFe}^{3+}\text{Si}_2\text{O}_6$ , respectively; the  $\epsilon_3$  component is instead very small and oriented around 30 ° from  $c$   
448 edge of Li-cpx (Fig. 8). The normalized strain components for  $\text{LiAlSi}_2\text{O}_6$  and  $\text{LiFe}^{3+}\text{Si}_2\text{O}_6$  are close  
449 to 1:0.78:0.14 and 1:0.95:0.23, respectively (Fig. 8).

450 The same comparison has been done with respect to pressure only for  $\text{LiAlSi}_2\text{O}_6$  that retains  
451 its  $C2/c$  space group with extended chains from ambient to pressure < 3.3 GPa (Arlt and Angel  
452 2000), whereas  $\text{LiFe}^{3+}\text{Si}_2\text{O}_6$  transforms from  $C2/c$  to  $P2_1/c$  at a relative low pressure < 1 GPa  
453 (Pommier et al. 2005). Similar to temperature, the effect of pressure induces an absolute  
454 deformation from room- to high- $P$  (3.2 GPa) of < 1 % per strain vectors. This deformation induces  
455 a contraction of strain tensor. The absolute magnitude of  $\epsilon_1$  and  $\epsilon_2$  are very similar, but  $\epsilon_3$  is close in  
456 % to these other two components, with normalized strain components close to 1:0.97:0.73 (Fig. 8).  
457 The strain tensor induced by pressure is completely different from that related to  $X$  and  $T$ ; the  $\epsilon_2$   
458 axes lies on  $b$  cell edge, whereas  $\epsilon_1$  and  $\epsilon_3$  are close to be normal and parallel to  $c$  side (Fig. 8). A  
459 general reappraisal of main features of lattice strains induced by  $X$ ,  $T$  and  $P$  for Li-cpx in the  $C2/c$   
460 stability field with extended tetrahedral chains is reported on top of Fig. 8. Li-cpx with M1-site  
461 progressively larger determine a significant increase in the  $\epsilon_1$  axis along  $b$ , whereas intermediate  
462 and low strain axes ( $\epsilon_2$  and  $\epsilon_3$ ) are nearly parallel to  $a$  and at about 30 ° from  $c$  (Fig. 8). The lattice  
463 strain induced by  $T$  will provoke a similar enlargement ( $\epsilon_1$  and  $\epsilon_2$ ) along  $b$  and  $a$  edges, whereas a  
464 minor elongation ( $\epsilon_3$ ) will be observed at about 30 ° from  $c$  (Fig. 8). The cell deformation induced  
465 by  $P$  will instead shorten all strain tensor components ( $\epsilon_1$ ,  $\epsilon_2$  and  $\epsilon_3$ ) with a similar % amount;

466 notably, high- $P$  is the only stress (also Al - Ni substitution will shorten along  $c$ , see before) that  
467 induces a strain component to be almost parallel to  $c$  edge (Fig. 8).

468 To gain further insight in the mechanism of deformation induced by chemical substitution  
469 (Fig. 8), we calculated the strain between Al-Fe<sup>3+</sup>, Fe<sup>3+</sup>-Sc and Sc-In and in addition that induced by  
470 the replacement of Li by Na in (Li,Na)Fe<sup>3+</sup>Si<sub>2</sub>O<sub>6</sub> compounds (Fig. 9). For the substitution at the  
471 M1-site (Al-Fe<sup>3+</sup>, Fe<sup>3+</sup>-Sc and Sc-In), it is invariably shown that  $\epsilon_1$  is coaxial with the  $b$  cell edge;  
472 conversely, either the strain tensor ratios and the orientation of  $\epsilon_2$  and  $\epsilon_3$  with respect to Li-cpx cell  
473 are different among them (Fig. 9). The replacement of Al by Fe<sup>3+</sup> imposes that intermediate and  
474 smallest  $\epsilon_2$  and  $\epsilon_3$  tensors are close to two thirds and half of the highest one ( $\epsilon_1$ ) respectively,  
475 oriented at about 100-105 ° and 10-15 ° from  $c$  edge, respectively. The substitution of Fe<sup>3+</sup> by Sc  
476 imposes that intermediate and lowest axes of strain tensors are 45 and 32 % of the maximum strain  
477 axis ( $\epsilon_1$ ) with an orientation at about 135 and 45 ° from the  $c$  direction (Fig. 9). The Sc-In cation  
478 substitutions are peculiar (Figs. 8 and 9) with the smallest strain component very close to 0 and  
479 almost co-axial with  $c$ , i.e. coaxial to the elongation of the tetrahedral chains, whereas the  
480 intermediate strain vector is aligned perpendicular to the T-chains and is about 40 % of the  
481 maximum strain axis ( $\epsilon_1$ ) lying along  $b$  (Fig. 9). The very limited deformation induced by Sc - In  
482 substitution along  $c$ , as already shown by cell edges saturation effects (Figs. 7 and 7s), evidence that  
483 fully stretched tetrahedral chains cannot be further extended. Sc and In are at the limit of a sixfold  
484 coordination in the M1 and the tetrahedral units are rather undeformable. In turn, the deformation of  
485 the cell induced by the replacement of Sc by In reaches a limiting value along the  $c$  axis and further  
486 expansion in cell volume must occur on other directions (Fig. 9). The substitution of Li by Na at the  
487 M2 site (considering <sup>VIII</sup>Li), with M1-site occupied only by Fe<sup>3+</sup>, unravels a very different behavior  
488 compared to any previous lattice deformation mechanisms (Figs. 8 and 9). The highest and lowest  
489 deformations occur on the  $ac$  plane, whereas the intermediate strain tensor is coaxial with the  $b$  cell  
490 edge; significantly, the  $\epsilon_2$  and  $\epsilon_3$  vectors are very similar in absolute modules, but the former is

491 positive and the latter is negative. In other words on the *ac* plane at about 30 ° from the direction of  
492 the tetrahedral chains the replacement of Li by Na induces a significant contraction (Fig. 9).

493 *Li-cpx average bond lengths.* The replacement of the smallest cation, Al with larger ones  
494 towards the largest, In, in Li-cpx also induces modifications of average bond lengths. Our XRPD  
495 data are unable to accurately determine single atomic bonds and bond angles, hence we compared  
496 only the average atomic bond lengths per site obtained here with those reported in previous studies  
497 performed with single-crystal X-ray diffraction method (Càmara et al. 2003; Kopylov et al. 2003;  
498 Redhammer and Roth 2004a, 2004b; Nestola et al. 2008). These average bond lengths are plotted in  
499 Fig. 10; the progressive substitution of Al towards In induces that M1-O average bond length  
500 increases of 10.6 % [ $\Delta\% = (\text{InM1-O}_{(\text{max})} - \text{AlM1-O}_{(\text{min})}) / \text{InM1-O}_{(\text{max})}$ ], M2-O of 4.3 %, whereas T-O  
501 are virtually unmodified, i.e. < 0.5 %.

502 Conversely, the strong T-O bonds are very slightly affected by the substitution of adjacent  
503 M1-site; as already pointed out, tetrahedrons accommodate this substitution by rotating themselves  
504 as rigid units (Redhammer and Roth 2004a). It is also worth noting that both M1- and M2-O  
505 average bonds increase linearly from Al to In, differently to cell parameters (Figs. 7, 7S and 10).  
506 The slight scatter from the general two linear regressions of our two Fe-richest Li-cpx (Fe#80 and  
507 Fe#100) can be attributed to a reduced accuracy of atomic positions determined by Rietveld (Table  
508 5), whereas the highest shifting from both linear M1- and M2-O regressions is observed for the  
509 LiVSi<sub>2</sub>O<sub>6</sub> compound (Redhammer and Roth 2004a). This feature couples with the singular low *T<sub>c</sub>*  
510 of LiVSi<sub>2</sub>O<sub>6</sub> compound (Redhammer and Roth 2004b) when compared with all other Li-cpx (see  
511 below).

512 *Steric effects in  $M^2Me^{1+M1}Me^{3+}Si_2O_6$  and  $M^2Me^{2+M1}Me^{2+}Si_2O_6$  cpx.* The substitution of  
513 cations at only M1- or M2-sites affects also the adjacent site occupied by the same cation (Figs. 6  
514 and 10). This “steric effect” was first reported in clinopyroxenes by Ghose et al. (1987) and recently  
515 expanded by Gori et al. (2015); in clinopyroxene, as well as for other silicate structures, the  
516 absolute shapes and sizes of all polyhedra can be also dependent to some extent on the interaction

517 with the adjacent polyhedra. Following Ghose et al (1987) and Gori et al (2015), and using a large  
518 and updating dataset of M1-O and M2-O average bond lengths, it is possible here to further  
519 highlight steric effects for the most important and key cpx crystal-chemical compositions and joins.  
520 For  ${}^{M2}Me^{1+M1}Me^{3+}Si_2O_6$  cpx, the increase of M1-O and M2-O average bond lengths induced by the  
521 same trivalent cation substitution ( ${}^{M1}Me^{3+}$ : Al from In, 0.535 to 0.800 Å,  $\Delta = 33\%$ ) for Li- and Na-  
522 cpx are very similar; in Li- and Na-cpx, M1-O increase of 10.6 and 10.1%, whereas M2-O of 4.3  
523 and 4.1 %, respectively (Fig. 11). Conversely, when the M1 site is kept occupied only by  $Fe^{3+}$  and  
524 the M2 site changes from Li to Na ( ${}^{M2}Me^{1+}$ :  ${}^{VIII}Li$  from Na, 0.92 to 1.18 Å,  $\Delta = 26\%$ ), the M1-O  
525 average lengths change lesser than 0.6 % and the M2-O of 3.4 % (Redhammer and Roth 2002), i.e.  
526 the steric effect of M2 site on M1 is very limited. Therefore, the structure of  ${}^{M2}Me^{1+M1}Me^{3+}Si_2O_6$   
527 cpx are much more affected by changes of  ${}^{M1}Me^{3+}$  than by  ${}^{M2}Me^{1+}$ , as clearly observable in Fig. 11.

528 This analysis can be extended to  ${}^{M2}Me^{2+M1}Me^{2+}Si_2O_6$  to have a more general reappraisal of  
529 the steric effect in clinopyroxene. When the M2-site is occupied only by Ca and the M1-site  
530 changes from Ni up to  $Mn^{2+}$  ( $Me^{2+}$ : Ni to Mn, 0.56 to 0.81 Å,  $\Delta = 31\%$ ) the M1-O average bond  
531 length increases of 4.7 % and induces a slight increase of 1.3 % in the M2-O mean length (Fig. 11).  
532 Hence, under a similar range of size differences of trivalent ( $Me^{3+}$  with  $\Delta = 33\%$ ) and divalent  
533 ( $Me^{2+}$  with  $\Delta = 31\%$ ) cations hosted at the M1-site, the M1-O and M2-O average bond lengths  
534 extend more than two times and the steric effect is by far more marked in  ${}^{M2}Me^{1+M1}Me^{3+}Si_2O_6$  than  
535  ${}^{M2}Me^{2+M1}Me^{2+}Si_2O_6$  cpx (Fig. 11). In contrast, when the substitution occur at M2-site for a fixed  
536 M1-site cation occupancy for  ${}^{M2}Me^{2+M1}Me^{2+}Si_2O_6$ , the situation is more complicated; when the M2-  
537 site is occupied by variable amounts of Ca-Mg, Ca- $Fe^{2+}$ , Ca-Co and Ca-Zn (considering average  
538 bond lengths for eight-fold coordination of the M2-site (in both  $C2/c$  and  $P2_1/c$  space groups) and  
539 the M1-site is occupied only by Mg,  $Fe^{2+}$ , Co and Zn, respectively, two general different situations  
540 are depicted (Alvaro et al., 2010, 2011; Gori et al. 2015). The substitution of Ca with Mg ( ${}^{VIII}Ca$   
541 and  ${}^{VIII}Mg$ : 1.12 to 0.89 Å, from  $Ca_1$  to  $Ca_{0.2}Mg_{0.8}$ ,  $\Delta = 16\%$ ) determines an increase of the M2-O  
542 mean lengths of only 1.5 %, whereas M1-O is little modified (0.5 %), i.e. the steric effect is very

543 low (Fig. 11); the substitution of Ca with Fe<sup>2+</sup> (<sup>VIII</sup>Ca and <sup>VIII</sup>Fe<sup>2+</sup>: 1.12 to 0.92 Å, from Ca<sub>1</sub> to Ca<sub>0.15</sub>  
544 Fe<sup>2+</sup><sub>0.85</sub>, Δ = 20 %) behaves similarly to that of Ca to Mg (Fig. 11) and the substitution of Ca with  
545 Co (<sup>VIII</sup>Ca and <sup>VIII</sup>Co: 1.12 to 0.9 Å, from Ca<sub>1</sub> to Ca<sub>0.4</sub>Co<sub>0.6</sub>, Δ = 12 %) determines an increase of the  
546 M2-O mean lengths of only 1.6 %, whereas M1-O is again weakly modified being 0.6 % (Fig. 11).  
547 The situation is instead significantly different for substitution of Ca with Zn (<sup>VIII</sup>Ca and <sup>VIII</sup>Zn: 1.12  
548 and 0.9 Å, from Ca<sub>1</sub> to Zn<sub>1.0</sub>, Δ = 20 %); this determines an increase in both M1-O and M2-O mean  
549 lengths of 2.2 and 2.0 %, i.e. both average lengths are faintly modified but with an almost identical  
550 rate (Fig. 11).

551 *Phase transitions in <sup>M2</sup>Li<sup>M1</sup>Me<sup>3+</sup>Si<sub>2</sub>O<sub>6</sub> cpx.* Crystal-chemistry of Li-cpx is probably one or  
552 even the best investigated sub-group of minerals at room-, low-, high-*T* and high-*P* (see before).  
553 Several general reappraisals have been thus inferred also the relation between symmetry and  
554 chemical compositions, i.e. the influence of crystal-chemical formulas of Li-cpx and the *P*<sub>21/c</sub>  
555 polymorph with kinked and relatively extended not-symmetrically equivalent tetrahedral chains  
556 and/or the two *C*<sub>2/c</sub> polymorphs with respectively extended and kinked symmetrically equivalent T-  
557 sites (Artl and Angel 2000; Càmara et al. 2003; Tribaudino et al. 2003, 2009; Redhammer and Roth  
558 2004b; Gatta et al. 2005; Pommier et al. 2005; Nestola et al. 2008; Periotto et al. 2013 and  
559 references therein).

560 However, the Li-cpx characterized in this study allow us to put further constraints on this  
561 topic. In Fig. 12 it is reported the space group of Li-cpx at ambient conditions plus the available  
562 stability fields at low- and high-*T* XRD of *P*<sub>21/c</sub> and *C*<sub>2/c</sub> (with extended T-chains) polymorphs; a  
563 similar plot as a function of *P* is not considered due to the limited amount of similar XRD data. In  
564 general, at room-*T* only M1-site hosting cations with a relative low size can crystallize with the  
565 *P*<sub>21/c</sub> space group; however, there is not a systematic behavior relating M1-site size and space  
566 group; in fact, LiNiSi<sub>2</sub>O<sub>6</sub> and Li(Al<sub>0.77</sub>Fe<sup>3+</sup><sub>0.23</sub>)Si<sub>2</sub>O<sub>6</sub> have practically the same dimensions, but the  
567 former is *P*<sub>21/c</sub> and the latter *C*<sub>2/c</sub> (Fig. 12). Similarly, *P*<sub>21/c</sub> LiCrSi<sub>2</sub>O<sub>6</sub> has a M1-site size  
568 intermediate between *C*<sub>2/c</sub> Li(Al<sub>0.43</sub>Fe<sup>3+</sup><sub>0.57</sub>)Si<sub>2</sub>O<sub>6</sub> and Li(Al<sub>0.15</sub>Fe<sup>3+</sup><sub>0.85</sub>)Si<sub>2</sub>O<sub>6</sub> (Fig. 12). Therefore, it

569 is definitively demonstrates that M1-site size only partially contributes to induce changes in crystal  
570 topology. Further and stringent evidences of this behavior are provided by the comparison between  
571  $\text{LiTiSi}_2\text{O}_6$  with  $\text{Li}(\text{Fe}^{3+}_{0.74}\text{Sc}_{0.26})\text{Si}_2\text{O}_6$  and  $(\text{Li}_{0.85}\text{Mg}_{0.06}\text{Fe}^{2+}_{0.09})(\text{Mg}_{0.15}\text{Fe}^{3+}_{0.85})\text{Si}_2\text{O}_6$ , as well as by  
572 the long known absence of a  $P2_1/c$  polymorph of Li-cpx with the smallest M1-size, i.e.  $\text{LiAlSi}_2\text{O}_6$   
573 (Fig. 12). The fact that clinopyroxene polymorphs do not exclusively switch their space group and  
574 arrangement of tetrahedral chains as a function of M2- and M1-site has been already proposed by  
575 Tribaudino et al. (2009) for Li-cpx and by Angel et al. (1998) for Mg-, Mn-, Cr- and  $\text{Fe}^{2+}$ -cpx. In  
576 turn, we can further stress that besides the M1-site effective ionic radii, also the electron  
577 configuration of trivalent cations in Li-cpx can play an important role on the existence (or not) of  
578 different polymorphs and of the occurrence of  $Tc$ ; this aspect could be also relevant for the M2-site.  
579 Here, it can be concluded that  $\text{Me}^{3+}$  cations with variable outer electron configurations impose  
580 different site size, distortions and eventual crystal field stability energies (CFSE); all these  
581 contributions are relevant of the stability of clinopyroxene polymorphs as a function of  $T$  and  $P$ .  
582 Further studies are required to model the relations among site size, valence electron arrangements  
583 and stability field of Li-cpx, as well for other mineral groups.

584

### 585 **Implications: detection of Li in natural pyroxenes**

586 Li cannot be detected by EPMA-WDS and/or SEM-EDS analyses standardly used in  
587 petrological studies; in parallel, Li being a light element, even if present with a relative significant  
588 a.p.f.u. in a clinopyroxene. For instance  $\text{Na}_{0.9}\text{Li}_{0.1}\text{Fe}^{3+}\text{Si}_2\text{O}_6$  is composed of 0.65, 12.16, 34.81 and  
589 52.38 wt.% of  $\text{Li}_2\text{O}$ ,  $\text{Na}_2\text{O}$ ,  $\text{Fe}_2\text{O}_3$  and  $\text{SiO}_2$ , respectively, and  $\text{Na}_{0.8}\text{Li}_{0.2}\text{Fe}^{3+}_{0.1}\text{Si}_2\text{O}_6$  is composed of  
590 1.28, 13.24, 34.12 and 51.35 wt.% of  $\text{Li}_2\text{O}$ ,  $\text{Na}_2\text{O}$ ,  $\text{Fe}_2\text{O}_3$  and  $\text{SiO}_2$ , respectively. Hence, its  
591 detection could be difficult even indirectly by difference to 100 wt.%, especially when both  $\text{Fe}^{2+}$   
592 and  $\text{Fe}^{3+}$  are present. By contrast, the accurate determination of cell parameters of an alkaline  
593 clinopyroxene mineral hosted in a rock can be performed quickly and used to constrain the presence  
594 of this light and elusive element, as already pointed out for Li-bearing amphiboles, where the M4-

595 site occupancy the corresponding M2-site in clinopyroxene) is well correlated with the  $\beta$  angle  
596 (Hawthorne et al. 1993; Iezzi et al. 2003b, 2006, 2010; Della Ventura et al. 2005). This is important  
597 for the semi-quantitative determination of chemical compositions of spodumene, especially the  
598 possible presence of  $\text{Fe}^{2+}$  vs  $\text{Fe}^{3+}$  and/or Na, that is used for extraction of Li (London 1984; Deer et  
599 al. 1997; Dill 2010). Jadeite and aegirine with ideal formula  $\text{NaAlSi}_2\text{O}_6$  and  $\text{NaFe}^{3+}\text{Si}_2\text{O}_6$ ,  
600 respectively, could incorporate some amount of Li at their M2 site, as shown by the near ideal solid  
601 solution investigated by Redhammer and Roth (2002) (Fig. 5); it is, therefore, important to  
602 constrain the actual amount of Li at M2-site for rocks containing alkali clinopyroxenes, especially  
603 for jadeite that is one of the most used mineral for geobarometric models (Deer et al. 1997).

604 The  $a$ ,  $b$ ,  $c$  and volume cell parameters vs their  $\beta$  angles for several clinopyroxene solid  
605 solutions with compositions accurately constrained are reported in Fig. 13. Similar to alkali  
606 amphiboles, also for clinopyroxenes the angular value of the  $\beta$  angle straightforward scales with  
607 cation type and abundance (and average cation size), whereas the M1-site occupancy very poorly or  
608 slightly influences this angular value for  $^{\text{M2}}\text{Me}^{1+\text{M1}}\text{Me}^{3+}\text{Si}_2\text{O}_6$  and  $^{\text{M2}}\text{Me}^{2+\text{M1}}\text{Me}^{2+}\text{Si}_2\text{O}_6$  (variable Mg  
609 and  $\text{Fe}^{2+}$  amounts at M1-site in diopside produces a shift in  $\beta$ ), respectively. Hence, these four plots  
610 show that Li-cpx have the highest  $\beta$  angle, Na-cpx the intermediate and Ca-cpx the lowest ones. The  
611 increasing of cation size at M1-site for  $^{\text{M2}}(\text{Na,Li})^{\text{M1}}\text{Me}^{3+}\text{Si}_2\text{O}_6$  cpx tends to shift the  $a$ ,  $b$ ,  $c$  and  
612 volume lattice parameters towards high value, leaving practically unchanged their  $\beta$  value, except  
613 for Li-cpx with a  $P2_1/c$  symmetry ( $\text{LiNiSi}_2\text{O}_6$  and  $\text{LiCrSi}_2\text{O}_6$ ) and  $\text{LiTiSi}_2\text{O}_6$ ; similarly, even a slight  
614 presence of  $\text{Fe}^{2+}$  and/or Mg at the M2-site in  $^{\text{M2}}(\text{Li,Fe}^{2+},\text{Mg})^{\text{M1}}(\text{Fe}^{3+},\text{Fe}^{2+},\text{Mg})\text{Si}_2\text{O}_6$  cpx shifts  
615 leftwards the  $\beta$  value (Fig. 13). Being that either  $b$  and volume parameters changes together with  $\beta$   
616 value for  $^{\text{M2}}(\text{Na,Li})^{\text{M1}}\text{Me}^{3+}\text{Si}_2\text{O}_6$  cpx, it can be valuable using these two plots to accurately  
617 determine the possible amounts of Li in jadeite-aegirine cpx, as well as to exploit the regression  
618 provided in Fig. 5 (Li a.p.f.u. vs  $\beta$  value) using the data of Redhammer and Roth (2002). To  
619 summarize, simple crystallographic data of cell parameters can accurately constrain (0.1/0.2  
620 a.p.f.u.) the presence of Li in natural clinopyroxenes.



621

622

### Acknowledgments

623

624 We warmly acknowledge the editorial handling of the D. G. Gatta, the fruitful suggestions  
625 of the Structures Editor that deeply enhanced the presentation of crystallographic data. We strongly  
626 appreciate the revisions of G.J. Redhammer and an anonymous reviewer, that enhanced the clarity  
627 of this study.

628 We would like to thank the interdepartmental laboratory of Electron Microscopy &  
629 Microanalysis, located at the Biology department of Patras University (Greece), for access to  
630 equipment and technical assistance. We would like to thank NanoMEGAS SPRL (Belgium) for  
631 technical support and funding for the research work related to Transmission Electron Microscopy.  
632 G.I. was supported by the “Fondi Ateneo of the University G. d'Annunzio of Chieti”.

633

634

### List of references

635 Alvaro, M., Nestola, F., Boffa-Ballaran, T., Càmara, F., Domeneghetti, M.C. and Tazzoli,  
636 V. (2010) High-pressure phase transition of a natural pigeonite. American Mineralogist 95, 300-  
637 311.

638 Alvaro, M., Càmara, F., Domeneghetti, M.C., Nestola, F. and Tazzoli, V. (2011) HT  $P2_1/c$ -  
639  $C2/c$  phase transition and kinetics of  $Fe^{2+}$ -Mg order-disorder of an Fe-poor pigeonite: implications  
640 for the cooling history of ureilites. Contributions to Mineralogy and Petrology 162 (3), 599-613.

641 Arlt, T., and Angel, R.J. (2000) Displacive phase transitions in C-centred clinopyroxenes:  
642 spodumene,  $LiScSi_2O_6$  and  $ZnSiO_3$ . Physics and Chemistry of Minerals, 27, 719-731.

643 Arlt, T., Angel, R.J., Miletich, R., Armbruster, T., and Peters, T. (1998) High-pressure  
644  $P2_1/c$ - $C2/c$  phase transitions in clinopyroxenes: Influence of cation size and electronic structure.  
645 American Mineralogist, 83, 1176–1181.

- 646 Arlt, T., Kunz, M., Stoltz, J., Armbruster, T., and Angel, R.J. (2000) P-T-X data on P21/c  
647 clinopyroxenes and their displacive phase transitions. Contributions to Mineralogy and Petrology,  
648 138, 35–45.
- 649 Bruno, E., Carbonin, S., and Molin, G. (1982). Crystal structures of Ca-rich clinopyroxenes  
650 on the  $\text{CaMgSi}_2\text{O}_6$  -  $\text{Mg}_2\text{Si}_2\text{O}_6$  join. TMPM Tschermaks Mineralogische und Petrographische  
651 Mitteilungen, 29, 223-240.
- 652 Bromiley, G.D., Keppler, H., McCammon, C., Bromiley, F. A. and Jabconsen, S. D. (2004)  
653 Hydrogen solubility and speciation in natural, gem-quality chromian diopside. American  
654 Mineralogist 89, 941-949.
- 655 Burla, M.C., Carrozzini, B., Cascarano, G.L., Giacovazzo, C., Mallamo, Mazzone, A., and  
656 Polidori, G. (2015) Crystal structure determination and refinement via SIR2014. Journal of Applied  
657 Crystallography 48, 306-309.
- 658 Brown, W.L. (1971) On lithium and sodium trivalent-metal pyroxenes and crystal-field  
659 effects. Mineralogical Magazine, 38,43-48.
- 660 Càmara, F., Iezzi, G., and Oberti, R. (2003) HT-XRD study of synthetic ferrian magnesian  
661 spodumene: the effect of site dimension on the  $P2_1/c \leftrightarrow C2/c$  phase transition. Physics and  
662 Chemistry of Minerals, 30, 20-30.
- 663 Càmara, F., Iezzi, G., Tiepolo, M., and Oberti, R. (2006) The crystal chemistry of lithium  
664 and  $\text{Fe}^{3+}$  incorporation in orthopyroxene. Physics and Chemistry of Minerals, 33, 475-483.
- 665 Cameron, M., Sueno, S., Prewitt, C.T., and Papike, J.J. (1973) High-temperature crystal  
666 chemistry of acmite, diopside, hedenbergite, jadeite, spodumene, and ureyite. American  
667 Mineralogist, 58, 594-618.
- 668 Deer, W.A., Howie, R.A., and Zussman, J. (1997) Single-chain silicates (volume 2A). The  
669 Geological Society of London, United Kingdom, 668 pp.

670 Della Ventura, G., Redhammer, G.J., Iezzi, G., , Hawthorne, F.C., Papin, A., and Robert J.-  
671 L. (2005) A Mössbauer and FTIR study of synthetic amphiboles along the magnesioriebeckite –  
672 ferri-clinoholmquistite join. *Physics and Chemistry of Minerals*, 32, 103-113.

673 Dill, H.G. (2010) The “chessboard” classification scheme of mineral deposits: Mineralogy  
674 and geology from aluminum to zirconium. *Earth-Science Reviews* 100, 1-420.

675 Gatta, G.D., Boffa Ballaran, T., and Iezzi, G. (2005) High-pressure X-ray and Raman study  
676 of a ferrian magnesian spodumene. *Physics and Chemistry of Minerals*, 32, 132-139.

677 Ghose, S., Wan, C., and Okamura, F.P. (1987) Crystal structures of  $\text{CaNiSi}_2\text{O}_6$  and  
678  $\text{CaCoSi}_2\text{O}_6$  and some crystal-chemical relations in  $C2/c$  clinopyroxenes. *American Mineralogist*,  
679 72, 375–381.

680 Gorelik, T.E., Stewart, A.A., and Kolb U. (2011) Structure solution with automated electron  
681 diffraction tomography data: different instrumental approaches. *Journal of Microscopy*, 244, 325-  
682 331.

683 Gori, C., Tribaudino, M., Mantovani, L., Delmonte, D. Mezzadri, F., Gilioli, E., and  
684 Calestani, G. (2015). Ca-Zn solid solutions in  $C2/c$  pyroxenes: Synthesis, crystal structure, and  
685 implications for Zn geochemistry. *American Mineralogist*, 100, 2209–2218.

686 Finger, L.W., Cox, D.E., and Jephcoat, A.P. (1994) A correction for powder diffraction peak  
687 asymmetry due to axial divergence. *Journal of Applied Crystallography*, 27, 892–900.

688 Hammersley, A.P., Svensson, S.O., Hanfland, M., Fitch, A.N., and Häusermann, D.  
689 (1996) Two-dimensional detector software: From real detector to idealised image or two-theta scan.  
690 *High Pressure Research*, 14, 235-248.

691 Hawthorne, F.C., Ungaretti, L., Oberti, R., and Bottazzi P. (1993) Li: An important  
692 component in igneous alkali amphiboles. *American Mineralogist*, 78, 733–745.

693 Higgins, M.D. (2006). *Quantitative Textural Measurements in Igneous and Metamorphic*  
694 *Petrology*. Cambridge University Press, Cambridge.

- 695 Iezzi, G., Della Ventura, G., Pedrazzi, G., Robert, J.-L., and Oberti, R. (2003a) Synthesis  
696 and characterisation of ferri-clinoferroholmquistite,  $\text{Li}_2\text{Fe}^{2+}_3\text{Fe}^{3+}_2\text{Si}_8\text{O}_{22}(\text{OH})_2$ . European Journal of  
697 Mineralogy, 15, 321-328.
- 698 Iezzi, G., Della Ventura, G., Càmara, F., Pedrazzi, G., and Robert, J.-L. (2003b) The  $^{\text{B}}\text{Na}$  –  
699  $^{\text{B}}\text{Li}$  exchange in A-site vacant amphiboles: synthesis and cation ordering along the ferri-  
700 clinoferroholmquistite – riebeckite join. American Mineralogist, 88, 955-961.
- 701 Iezzi, G., Boffa-Ballaran, T., McCammon, C., and Langenhorst, F. (2005) The  $\text{CaGeO}_3$ -  
702  $\text{Ca}_3\text{Fe}_2\text{Ge}_3\text{O}_{12}$  garnet solid solution. Physics and Chemistry of Minerals, 32, 197-207.
- 703 Iezzi, G., Della Ventura, G., and Tribaudino M. (2006). Synthetic  $P2_1/m$  amphiboles in the  
704 system  $\text{Li}_2\text{O}-\text{Na}_2\text{O}-\text{MgO}-\text{SiO}_2-\text{H}_2\text{O}$  (LNMSH). American Mineralogist, 91, 425-429.
- 705 Iezzi, G., Mollo, S., Ventura, G., Cavallo, A., and Romano, C., (2008). Experimental  
706 solidification of anhydrous latitic and trachytic melts at different cooling rates: the role of  
707 nucleation kinetics. Chemical geology, 253, 91-101.
- 708 Iezzi, G., Della Ventura, G., Tribaudino, M., Nemeth, P., Margiolaki, I., Cavallo, A.,  
709 Gaillard, F., and Behrens, H. (2010) Phase transition induced by solid-solution: the  $^{\text{B}}\text{Ca}$ - $^{\text{B}}\text{Mg}$   
710 substitution in richteritic amphiboles. American Mineralogist, 95, 369-381.
- 711 Iezzi, G., Mollo, S., Torresi, G., Ventura, G., Cavallo, A., and Scarlato, P. (2011a)  
712 Experimental solidification of an andesitic melt by cooling. Chemical Geology, 283, 261–273.
- 713 Iezzi, G., Tribaudino, M., Della Ventura, G., and Margiolaki, I. (2011b) The high  
714 temperature  $P2_1/m$  –  $C2/m$  phase transition in synthetic amphiboles along richterite – ( $^{\text{B}}\text{Mg}$ )-  
715 richterite join. American Mineralogist, 96, 353-363.
- 716 Iezzi, G., Mollo, S., Shahini, E., Cavallo, A., and Scarlato, P. (2014) The cooling kinetics of  
717 plagioclase feldspars as revealed by electron-microprobe mapping. American Mineralogist 99, 898–  
718 907.
- 719 Kolb, U., Gorelik, T., Kübel, C., Otten, M. T., and Hubert, D. (2007) Towards automated  
720 diffraction tomography: Part I - Data acquisition. Ultramicroscopy 107, 507-513.

721 Labiche, J.-C., Mathon, O., Pascarelli, S., Newton, M.A., Ferre, G.G., Curfs, C., Vaughan,  
722 G., Homs, A., and Carreiras, D.F.. (2007) The fast readout low noise camera as a versatile x-ray  
723 detector for time resolved dispersive extended x-ray absorption fine structure and diffraction studies  
724 of dynamic problems in materials science, chemistry, and catalysis. Review of Scientific  
725 Instruments, 78, 091301.

726 Lanzafame, G., Mollo, S., Iezzi, G., Ferlito, C., and Ventura, G. (2013) Unraveling the  
727 solidification path of a pahoehoe “cicirara” lava from Mount Etna volcano. Bulletin of  
728 Volcanology, 75, 703.

729 Larson, A.C. and Von Dreele, R.B. (1997) GSAS: General structure analysis system. Los  
730 Alamos National Laboratory Report LAUR 86-748.

731 Le Bail, A. (2005) Whole powder pattern decomposition methods and applications: A  
732 retrospection. Powder Diffraction, 20, 316–326.

733 London, D. (1996) Granitic pegmatites. Transactions of the Royal Society of Edinburgh,  
734 Earth Sciences.

735 Mantovani, L., Tribaudino, M., Mezzadri, F., Calestani, G., and Bromiley, G. (2013) The  
736 structure of (Ca,Co)CoSi<sub>2</sub>O<sub>6</sub> pyroxenes and the Ca-M<sup>2+</sup> substitution in (Ca,M<sup>2+</sup>)M<sup>2+</sup>Si<sub>2</sub>O<sub>6</sub>  
737 pyroxenes (M<sup>2+</sup>= Co, Fe, Mg). American Mineralogist, 98, 1241–1252.

738 Mantovani, L., Tribaudino, M., Bertoni, G., Salviati, G., and Bromiley, G. (2014) Solid  
739 solutions and phase transitions in (Ca,M<sup>2+</sup>)M<sup>2+</sup>Si<sub>2</sub>O<sub>6</sub> pyroxenes (M<sup>2+</sup>= Co, Fe, Mg). American  
740 Mineralogist, 99, 704–711.

741 Mugnaioli, E., Gorelik, T. and Kolb, U. (2009) “*Ab initio*” structure solution from electron  
742 diffraction data obtained by a combination of automated diffraction tomography and precession  
743 technique. Ultramicroscopy 109, 758–765.

744 Nestola, F., Tribaudino M., Boffa Ballaran, T., Liebske C., and Bruno M. (2007) The crystal  
745 structure of pyroxenes along the jadeite-hedenbergite and jadeite-aegirine joins. American  
746 Mineralogist, 92: 1492-1501.

747 Nestola, F., Boffa Ballaran, T., and Ohashi, H. (2008) The high-pressure  $C2/c-P2_1/c$  phase  
748 transition along the  $\text{LiAlSi}_2\text{O}_6$ – $\text{LiGaSi}_2\text{O}_6$  solid solution. *Physics and Chemistry of Minerals*, 35,  
749 477–484.

750 Nestola, F., Redhammer, G.J., Pamato, M.G., Secco, L., and Dal Negro, A. (2009) High-  
751 pressure phase transformation in  $\text{LiFeGe}_2\text{O}_6$  pyroxene. *American Mineralogist*, 94, 616–621.

752 Ohashi H, Osawa T, and Sato A (2003) Crystal structures of  $\text{Li}(\text{Al,Ga})\text{Si}_2\text{O}_6$  pyroxenes. In:  
753 Ohashi H (ed.) X-ray study on Si-O bonding. Publishing Service Center, Tokyo, pp 146–158. ISBN  
754 4-89630-094-7.

755 Periotto, B., Angel, R.J., Nestola, F., Balic-Zunic, T., Fontana, C., Pasqual, D., Alvaro, M.,  
756 and Redhammer G.J. (2013) High-pressure X-ray study of  $\text{LiCrSi}_2\text{O}_6$  clinopyroxene and the  
757 general compressibility trends for Li-clinopyroxenes. *Physics and Chemistry of Minerals*, 40, 387-  
758 399.

759 Pommier, C.J.S., Downs, R.T., Stimpfl, M., Redhammer, G.J., and Denton, M.B. (2005)  
760 Raman and X-ray investigations of  $\text{LiFeSi}_2\text{O}_6$  pyroxene under pressure. *Journal of Raman*  
761 *Spectroscopy*, 36, 864–871.

762 Raudsepp, M., Hawthorne, F.C. and Turnock, A. (1990) Crystal chemistry of synthetic  
763 pyroxenes on the join  $\text{CaNiSi}_2\text{O}_6$  -  $\text{CaMgSi}_2\text{O}_6$  (diopside): a Rietveld structure refinement study.  
764 *American Mineralogist*, 75, 1274-1281.

765 Redhammer, G.J., Roth, G., Paulus, W., Andre, G., Lottermoser, W., Amthauer, G.,  
766 Treutmann, W., and Koppelhuber-Bitschnau, B. (2001) The crystal and magnetic structure of Li-  
767 aegirine  $\text{LiFe}^{3+}\text{Si}_2\text{O}_6$ : a temperature-dependent study. *Physics and Chemistry of Minerals*, 28, 337–  
768 346.

769 Redhammer, G.J., Roth G. (2002) Structural variations in the aegirine solid-solution series  
770  $(\text{Na,Li})\text{FeSi}_2\text{O}_6$  at 298 K and 80 K. *Zeitschrift für Kristallographie*, 217, 1-10.

771 Redhammer, G.J. and Roth, G. (2004a) Structural variation and crystal chemistry of  
772  $\text{LiMe}^{3+}\text{Si}_2\text{O}_6$  clinopyroxenes Me = Al, Ga, Cr, V, Fe, Sc and In. Zeitschrift für Kristallographie,  
773 219, 278–294.

774 Redhammer, G.J. and Roth, G. (2004b) Structural changes upon the temperature dependent  
775  $C2/c \rightarrow P2_1/c$  phase transition in  $\text{LiMe}^{3+}\text{Si}_2\text{O}_6$  clinopyroxenes, Me = Cr, Ga, Fe, V, Sc and In.  
776 Zeitschrift für Kristallographie, 219, 585–605.

777 Redhammer, G.J., Amthauer G., Roth, G., Tippelt, G., and Lottermoser W. (2006) Single  
778 crystal X-ray diffraction and temperature dependent and  $^{57}\text{Fe}$  Mössbauer spectroscopy on the  
779 hedenbergite-aegirine  $(\text{Ca},\text{Na})(\text{Fe}^{2+},\text{Fe}^{3+})\text{Si}_2\text{O}_6$  solid solution. American Mineralogist, 91, 1271-  
780 1292.

781 Redhammer, G.J., Roth, G., Treutmann, W., Hoelzel, M., Paulus, W., Andre, G., Pietzonka,  
782 C., and Amthauer, G. (2009) The magnetic structure of clinopyroxene-type  $\text{LiFeGe}_2\text{O}_6$  and revised  
783 data on multiferroic  $\text{LiFe}^{3+}\text{Si}_2\text{O}_6$ . Journal of Solid State Chemistry, 182, 2374–2384.

784 Redhammer, G.J., Cámara, F., Alvaro, M., Nestola, F., Tippelt, G., Prinz, S., Simons, J.,  
785 Roth, G., and Amthauer, G. (2010) Thermal expansion and high-temperature  $P2_1/c$ - $C2/c$  phase  
786 transition in clinopyroxene-type  $\text{LiFeGe}_2\text{O}_6$  and comparison to  $\text{NaFe}(\text{Si},\text{Ge})_2\text{O}_6$ . Physics and  
787 Chemistry of Minerals, 37, 685–704.

788 Toby, B.H. (2001) EXPGUI, a graphical user interface for GSAS. Journal of Applied  
789 Crystallography, 34, 210–213.

790 Tribaudino, M., Nestola, F., Prencipe, M., and Rundlof, H. (2003) A single-crystal neutron-  
791 diffraction investigation of spodumene at 54 K. Canadian Mineralogist, 41, 521-527.

792 Tribaudino, M., Nestola, F., and Meneghini, C. (2005) Rietveld refinement of  
793 clinopyroxenes with intermediate Ca-content along the join diopside-enstatite. The Canadian  
794 Mineralogist, 43, 1411-1421.

795 Tribaudino, M., Bromiley, G., Ohashi, H., and Nestola, F. (2009) Synthesis, TEM  
796 characterization and thermal behaviour of LiNiSi<sub>2</sub>O<sub>6</sub> pyroxene. Physics and Chemistry of  
797 Minerals, 36, 527–536.

798 Tribaudino, M., and Mantovani L. (2014) Thermal expansion in C2/c pyroxenes: a review  
799 and new high temperature structural data on a pyroxene of composition (Na<sub>0.53</sub>Ca<sub>0.47</sub>)(  
800 Al<sub>0.53</sub>Fe<sub>0.47</sub>)Si<sub>2</sub>O<sub>6</sub> (Jd<sub>53</sub>Hd<sub>47</sub>). Mineralogical Magazine, 78, 311-324.

801 Ullrich A, Miletich R, Balic'-Zunic' T, Olsen L, Nestola F, Wildner M, and Ohashi H  
802 (2010) (Na,Ca)(Ti,Mg)Si<sub>2</sub>O<sub>6</sub> clinopyroxenes at high pressures: influence of cation substitution on  
803 elasticity and phase transition. Physics and Chemistry of Minerals, 37, 25-43.

804 Vetere, F., Iezzi, G., Behrens, H., Cavallo, A., Misiti, V., Dietrich, M., Knipping, J.,  
805 Ventura, G., and Mollo, S., (2013) Intrinsic solidification behavior of basaltic to rhyolitic melts: a  
806 cooling rate experimental study. Chemical Geology, 354, 233–242.

807 Vetere, F., Iezzi, G., Behrens, H., Holts, F., Ventura, G., Misiti, V., Cavallo, A., Mollo, S.,  
808 and Dietrich, M., (2015) Glass forming ability and crystallization behavior of sub-alkaline silicate  
809 melts. Earth-Science Reviews 150: 25-44.

810 Zhou, S.G, David, O., Moulay, T., Sougrati, M.T., and Melota B.C. (2014) Low temperature  
811 preparation and electrochemical properties of LiFeSi<sub>2</sub>O<sub>6</sub>. Journal of The Electrochemical Society,  
812 161, A1642-A1647.

813

814

815

816

817

818

819

820



821

822

823

824

825

826

827

828

829

830

831

832

833

834

835

836

### Figure captions

837 Figure 1. Textural features of the eight run-products analysed by back-scattered scanning  
838 electron microscopy (BS-SEM); labels of run-products, experimental conditions, their paragenesis  
839 and clinopyroxene nominal and measured compositions are reported in Tables 1 and 3; in the Fe#0  
840 run-product the light grey phase is corundum (plus a very low amount of  $\text{Al}_2\text{SiO}_5$ ), in the Fe#2+  
841 run-product the white phases is magnetite, whereas in the other run-products the white phase is  
842 hematite (Table 3); Fe- and Al-bearing clinopyroxenes show intermediate grey tones indicative of  
843 slight inter- and intra-crystalline variable compositions.

844

845 Figure 2. (top) Differences in Al occupancy at M1-site between nominal and measured by  
846 Rietveld refinement on synchrotron XRPD patterns. (bottom) Phase amounts in weight % (left) and

847 area % (right) determined by Rietveld refinement on synchrotron XRPD patterns and image  
848 analysis on back-scattered SEM data, respectively (see Table 3). The amount of Al (a.p.f.u.) is  
849 obtained by Rietveld refinement at the M1-site (Al = 1 - Fe), while M2- and T-site are occupied  
850 only by Li and Si, respectively.

851

852 Figure 3. Projections of the extracted intensities obtained from SAED patterns of the Fe#50  
853 run-product. Figures illustrate projections of  $b^*$  direction. The size of spots is proportional to the  
854 intensity. White spots correspond to the extracted intensity from the experimental data, whereas red  
855 spots illustrate the reflections representing (a) a centering, (b) b centering, (c) c centering, (d) c  
856 glide plane perpendicular to the b axis direction, (e)  $2_1$  screw axis along the b axis direction, for the  
857 reported cell. Panels a & b show that the experimental data violate the extinction conditions for  
858 these types of centering, thus c centering describes better the reciprocal space. Moreover panel d is  
859 indicative that  $C2/c$  space group is the right one. All figures were generated using the ADT3D  
860 software (NanoMEGAS SPRL, Belgium).

861

862 Figure 4. The synchrotron XRPD patterns (except Fe#50) collected on image plates. The  
863 Debye rings are more uniform and well defined moving from Fe#100 to Fe#0.

864

865 Figure 4S (supplementary material). The Fe#0 (up) and Fe#50 (down) synchrotron XRPD  
866 patterns refined by the Rietveld method. Black crosses and red lines are the observed and calculated  
867 XRPD patterns, respectively; the green and blue lines are background and residual between  
868 observed and calculated XRPD patterns, respectively.

869

870 Figure 5. (left column) Evolution of cell parameters as a function of the  $M^I$ Al measured by  
871 Rietveld refinements between  $LiAlSi_2O_6$  and  $LiFe^{3+}Si_2O_6$  (plus linear regressions and equations);  
872 the red circles are the data of the FE#2+ run-product and the blue crosses are SC-XRD data from

873 Redhammer and Roth (2004); (right column) The SC-XRD data of Redhammer and Roth (2002)  
874 between  $\text{LiFe}^{3+}\text{Si}_2\text{O}_6$  and  $\text{NaFe}^{3+}\text{Si}_2\text{O}_6$  are also reported (green triangles) as a comparison (plus  
875 linear regressions and equations). The evolution of both cell volume parameters are almost linear,  
876 suggesting ideal solid solutions between  $\text{M}^1\text{Al}$  and  $\text{M}^1\text{Fe}^{3+}$  and  $\text{M}^2\text{Li}$  and  $\text{M}^2\text{Na}$  of Li-cpx. The relative  
877 variations (%) are calculated as:  $(\text{max}-\text{min})/\text{max}$ . The substitution of Al with  $\text{Fe}^{3+}$  and Li with Na  
878 induce an increasing (from low to high %) of  $c$ ,  $a$ ,  $b$ ,  $V$  with  $\beta$  unmodified and of  $b$ ,  $\beta$ ,  $V$  with  $c$  plus  
879  $a$  almost un-affected, respectively.

880

881 Figure 6. Evolution of average bond lengths (top: M2-site, middle: M1-site, bottom: T-site)  
882 as a function of the  $\text{M}^1\text{Al}$  (a.p.f.u.) measured by Rietveld refinements (black circles); the linear  
883 regressions are performed only on the samples of this study, whereas the blue crosses are reported  
884 with comparison with our data (single-crystal X-ray diffraction data from Redhammer and Roth,  
885 2004). The substitution of Al by  $\text{Fe}^{3+}$  at the M1-site mainly affect the M1-O and to a lesser extent  
886 the M2-O average bond lengths, respectively, whereas the T-site is only slightly modified. The  
887 relative variations (%) are calculated as:  $(\text{max}-\text{min})/\text{max}$ .

888 Figure 7. Evolution of cell volume at 298 K as a function of the average cation size at the  
889 M1-site of  $\text{LiMe}^{3+}\text{Si}_2\text{O}_6$  clinopyroxenes; filled symbols are  $C2/c$  clinopyroxenes, whereas open  
890 ones are  $P2_1/c$  crystals with available temperature of  $P2_1/c - C2/c$  phase transitions. The other cell  
891 parameters are reported in the supplementary materials (Fig. 7S). The relative variations (%) are  
892 calculated as:  $(\text{max}-\text{min})/\text{max}$ .

893

894 Figure 7S (to be deposited as supplementary material). From top to bottom: evolution of cell  
895 edges,  $\beta$  angle and  $a\sin(\beta)$  at 298 K as a function of the average cation size at the M1-site of  
896  $\text{LiMe}^{3+}\text{Si}_2\text{O}_6$  clinopyroxenes and  $(\text{Li}_{0.85}\text{Mg}_{0.09}\text{Fe}^{2+}_{0.06})(\text{Fe}^{3+}_{0.85}\text{Mg}_{0.15})\text{Si}_2\text{O}_6$ ; filled and open symbols  
897 indicate  $C2/c$  and  $P2_1/c$  clinopyroxenes, respectively. Symbols are those of Fig. 7. The relative  
898 variations (%) are calculated as:  $(\text{max}-\text{min})/\text{max}$ .

899

900 Figure 8. Finite lattice strain (rectangular plots) and orientation (semi-circular plots) of  
901 principal strain axes of  $C2/c$   $\text{Li}^{\text{M1}}\text{Me}^{3+}\text{Si}_2\text{O}_6$  pyroxenes, plus two  $P2_1/c$   $\text{M}^{\text{M1}}\text{Ni}$  and  $\text{M}^{\text{M1}}\text{Cr}$  reported as  
902 empty symbols, induced by chemical substitution (left column of graphs), temperature and pressure  
903 (middle and right columns of graphs). The lattice strain induced by the ideal substitution was  
904 calculated from  $\text{M}^{\text{M2}}\text{Li}^{\text{M1}}\text{AlSi}_2\text{O}_6$  to  $\text{Li}^{\text{M1}}\text{Me}^{3+}\text{Si}_2\text{O}_6$ , where Me is a progressive large cation, i.e.  $\text{M}^{\text{M1}}\text{Al}$   
905 vs  $\text{M}^{\text{M1}}\text{In}$ ; cell parameters of  $\text{Li}(\text{Al},\text{Fe}^{3+})\text{Si}_2\text{O}_6$  are from this study,  $\text{LiNiSi}_2\text{O}_6$  from Tribaudino et al.  
906 (2009),  $\text{LiTiSi}_2\text{O}_6$  from Kohn et al. (2009),  $\text{Li}(\text{Cr},\text{Ga},\text{V},\text{Sc},\text{In})\text{Si}_2\text{O}_6$  from Redhammer and Roth  
907 (2004a). Cell parameters of  $\text{LiAlSi}_2\text{O}_6$  and  $\text{LiFe}^{3+}\text{Si}_2\text{O}_6$  at high- $T$  are from Cameron et al. (1973)  
908 and Redhammer et al. (2001), respectively. Cell parameters of  $\text{LiAlSi}_2\text{O}_6$  at high- $P$  are from Arlt  
909 and Angel (2000).

910

911 Figure 9. Finite lattice strain (rectangular plots) and orientation (semi-circular plots) of  
912 principal strain axes of three sub-sets of  $C2/c$   $\text{Li}^{\text{M1}}\text{Me}^{3+}\text{Si}_2\text{O}_6$  (reported in Fig. 8) and one  $C2/c$   
913  $\text{M}^{\text{M1}}(\text{Li},\text{Na})\text{Fe}^{3+}\text{Si}_2\text{O}_6$  pyroxenes. From left to right, the lattice strain for each sub-set was calculated  
914 for four compositions between  $\text{Al-Fe}^{3+}$  (data from this study),  $\text{Li-Na}$  (data from Redhammer and  
915 Roth, 2002),  $\text{Fe}^{3+}\text{-Sc}$  and  $\text{Sc-In}$  (data from Redhammer and Roth, 2004a). The schematic  $\epsilon_1$ ,  $\epsilon_2$  and  
916  $\epsilon_3$  (top) lattice strains induced by these four cation substitutions are reported their schematic  
917 orientation and the crystal structure of spodumene on the  $a$ - $c$  and  $a$ - $b$  planes. The relative  $\Delta$   
918 variations (%) are calculated as:  $(\text{max}-\text{min})/\text{max}$ .

919

920 Figure 10. Evolution of M2- (up), M1- (middle) and T- (bottom) O average bond lengths at  
921 298 K as a function of the average cation size at the M1-site of  $\text{LiMe}^{3+}\text{Si}_2\text{O}_6$  clinopyroxenes. The  
922 relative variations (%) are calculated as:  $(\text{max}-\text{min})/\text{max}$ .

923

924 Figure 11. Trends of average M2-O (considering  $^{\text{VIII}}\text{Me}^{1+}$  and  $^{\text{VIII}}\text{Me}^{2+}$  at M2-site) versus  
925 M1-O (considering  $^{\text{VI}}\text{Me}^{2+}$  and  $^{\text{VI}}\text{Me}^{3+}$  at M1-site) bond lengths of different clinopyroxenes, as a  
926 function of cation substitution occurring a) only at M1-site by trivalent cations with M2-site  
927 occupied only by Li (black circles) or Na (red squares), b) only at M1-site by divalent cations with  
928 M2-site occupied only by Ca (violet crosses) and c) only at M2-site by Ca and another divalent  
929 cations (Mg, Co and Zn) with M1-site occupied only by the same divalent cation hosted in M2-site  
930 together with Ca (Mg: orange diamonds, Co: blue upward triangles, Zn: green downward triangles).

931

932 Figure 12. Relations among average cation size at the M1-site of  $\text{LiMe}^{3+}\text{Si}_2\text{O}_6$   
933 clinopyroxenes, space group and  $T_c$  ( $T$  of phase transitions from  $C2/c$  and  $P2_1/c$ ). Full and open  
934 symbols are  $C2/c$  and  $P2_1/c$  at room- $T$ , respectively. Thin-yellow and thick-grey vertical bars refer  
935 to  $C2/c$  and  $P2_1/c$  space groups at non-ambient  $T$  as investigated by XRD data, respectively.  
936  $\text{Li}(\text{Al},\text{Fe}^{3+})\text{Si}_2\text{O}_6$  at room- $T$  are from this study,  $\text{LiTiSi}_2\text{O}_6$  at room- $T$  from Kopnin et al. (2009),  
937  $\text{LiNiSi}_2\text{O}_6$  at high- $T$  from Tribaudino et al. (2009),  $\text{Li}(\text{Al},\text{Cr},\text{Ga},\text{V},\text{Fe}^{3+},\text{Sc},\text{In})\text{Si}_2\text{O}_6$  at high- and  
938 low- $T$  from Redhammer and Roth (2004b),  $(\text{Li}_{0.85}\text{Mg}_{0.09}\text{Fe}^{2+}_{0.06})(\text{Mg}_{0.15},\text{Fe}^{3+}_{0.85})\text{Si}_2\text{O}_6$  at high- $T$   
939 Càmara et al. (2003). This plot straightforwardly shows that M1-site dimension only partially rules  
940 out the symmetry of Li-cpx; valence electrons and site distortions of trivalent cation at the M1-site  
941 also strongly affects the space group and potential  $T_c$ .

942

943 Figure 13.  $\beta$  vs  $a$ ,  $b$ ,  $c$  and volume cell parameters for clinopyroxenes of joins:  
944  $\text{Li}(\text{Al},\text{In})\text{Si}_2\text{O}_6$  from this study, Redhammer and Roth (2004a) and Tribaudino et al. (2009) (black  
945 dots);  $\text{LiTiSi}_2\text{O}_6$  from Kopnin et al. (2003) (black-pink circle);  $(\text{Li}_{1-x}\text{M}^{2+}_x)(\text{M}^{2+}_x\text{Fe}^{3+}_{1-x})\text{Si}_2\text{O}_6$  ( $\text{M}^{2+}$  =  
946 Mg or Fe,  $x \leq 0.15$ ) from this study and Càmara et al. (2003) (red stars);  $(\text{Li}_{1-x}\text{Na}_x)\text{Fe}^{3+}\text{Si}_2\text{O}_6$  ( $0 \leq x$   
947  $\leq 1$ ) from Redhammer and Roth (2002) (green triangles);  $(\text{Ca}_{1-x}\text{Na}_x)(\text{Fe}^{2+}_{1-x}\text{Fe}^{3+}_x)\text{Si}_2\text{O}_6$  ( $0 \leq x \leq 1$ )  
948 from Redhammer et al. (2006) (orange squares);  $\text{Ca}(\text{Fe}^{2+}_{1-x}\text{Mg}_x)\text{Si}_2\text{O}_6$  ( $0.5 \leq x \leq 1$ ) from  
949 Redhammer et al. (2006) and Raudsepp et al. (1990) (blue diamonds);  $\text{Na}(\text{Fe}^{3+}_{1-x}\text{Al}_x)\text{Si}_2\text{O}_6$  ( $0 \leq x \leq$

950 1) from Nestola et al. (2006) (brown crosses). Open symbols are  $P2_1/c$  clinopyroxenes ( $\text{LiNiSi}_2\text{O}_6$   
951 and  $\text{LiCrSi}_2\text{O}_6$ ) at room conditions. The bottom-right diagrams highlights the most common  
952 chemical substitutions occurring in natural Li-cpx. Similar to the original plot of Brown (1971),  
953 these diagrams readily and accurately discriminate Li amount in clinopyroxene, as well as cation  
954 occupancy at the M1 and M2 sites.

955

956

957

958

959

960

961

962

963

964

965

sample label	nominal formula (a.p.f.u.)	solid/H <sub>2</sub> O <sub>2</sub> (wt.%)	<i>T</i> (°C)	<i>P</i> (GPa)	duration (day)
Fe#0	LiAlSi <sub>2</sub> O <sub>6</sub>	9:1	800	2	3
Fe#20	Li(Al <sub>0.8</sub> Fe <sup>3+</sup> <sub>0.2</sub> )Si <sub>2</sub> O <sub>6</sub>	9:1	800	2	3
Fe#40	Li(Al <sub>0.6</sub> Fe <sup>3+</sup> <sub>0.4</sub> )Si <sub>2</sub> O <sub>6</sub>	9:1	800	2	3
Fe#50	Li(Al <sub>0.5</sub> Fe <sup>3+</sup> <sub>0.5</sub> )Si <sub>2</sub> O <sub>6</sub>	9:1	800	2	3
Fe#60	Li(Al <sub>0.4</sub> Fe <sup>3+</sup> <sub>0.6</sub> )Si <sub>2</sub> O <sub>6</sub>	9:1	800	2	3
Fe#80	Li(Al <sub>0.2</sub> Fe <sup>3+</sup> <sub>0.8</sub> )Si <sub>2</sub> O <sub>6</sub>	9:1	800	2	3
Fe#100	LiFe <sup>3+</sup> Si <sub>2</sub> O <sub>6</sub>	9:1	800	2	3
Fe#2+	LiFe <sup>3+</sup> Si <sub>2</sub> O <sub>6</sub>	intrinsic <i>f</i> O <sub>2</sub>	800	2	3

Table 2. Synchrotron powder diffraction data collection and refinement parameters.								
sample label	$\lambda$ (Å)	$2\theta$ (°) range	$2\theta$ (°) step	$d$ (Å) range	no. of points	no. of refined parameters	$R_p$	$R_{wp}$
Fe#0	0.325802	3.5 – 31.7	0.004	0.597 – 5.236	7050	72	0.028	0.024
Fe#20	0.325802	3.5 – 31.7	0.004	0.597 – 5.236	7050	76	0.055	0.045
Fe#40	0.325802	3.5 – 31.7	0.004	0.597 – 5.236	7050	74	0.040	0.034
Fe#50	0.325802	3.5 – 31.7	0.004	0.597 – 5.236	7050	71	0.030	0.029
Fe#60	0.325802	3.5 – 31.7	0.004	0.597 – 5.236	7050	69	0.032	0.029
Fe#80	0.325802	3.5 – 31.7	0.004	0.597 – 5.236	7050	69	0.041	0.033
Fe#100	0.325802	3.5 – 31.7	0.004	0.597 – 5.236	7050	72	0.072	0.046
Fe#2+	0.325802	3.5 – 31.7	0.004	0.597 – 5.236	7050	-	-	-

Footnotes:  $R_p = \sum |y_{obs} - y_{calc}| / \sum y_{obs}$  and  $R_{wp} = [\sum w(y_{obs} - y_{calc})^2 / \sum w y_{obs}^2]^{1/2}$  refer to Rietveld refinements. The run-product Fe#2+ was refined only by the Le Bail method.



Table 3. Synchrotron XRPD data and image analysis data						
sample label	<sup>‡</sup> actual formula (a.p.f.u.)	<sup>*</sup> space group	% of phases	pyroxene	corundum	hematite
Fe#0	LiAlSi <sub>2</sub> O <sub>6</sub>	C2/c	<sup>#</sup> by weight <sup>§</sup> by area	92 95	8 5	- -
Fe#20	Li(Al <sub>0.86</sub> Fe <sup>3+</sup> <sub>0.14</sub> )Si <sub>2</sub> O <sub>6</sub>	C2/c	<sup>#</sup> by weight <sup>§</sup> by area	92 94	5 1	3 5
Fe#40	Li(Al <sub>0.77</sub> Fe <sup>3+</sup> <sub>0.23</sub> )Si <sub>2</sub> O <sub>6</sub>	C2/c	<sup>#</sup> by weight <sup>§</sup> by area	87 93	1 -	12 7
Fe#50	Li(Al <sub>0.65</sub> Fe <sup>3+</sup> <sub>0.35</sub> )Si <sub>2</sub> O <sub>6</sub>	C2/c	<sup>#</sup> by weight <sup>§</sup> by area	89 91	- -	11 9
Fe#60	Li(Al <sub>0.43</sub> Fe <sup>3+</sup> <sub>0.57</sub> )Si <sub>2</sub> O <sub>6</sub>	C2/c	<sup>#</sup> by weight <sup>§</sup> by area	87 95	- -	13 5
Fe#80	Li(Al <sub>0.15</sub> Fe <sup>3+</sup> <sub>0.85</sub> )Si <sub>2</sub> O <sub>6</sub>	C2/c	<sup>#</sup> by weight <sup>§</sup> by area	92 93	- -	8 7
Fe#100	Li Fe <sup>3+</sup> Si <sub>2</sub> O <sub>6</sub>	C2/c	<sup>#</sup> by weight <sup>§</sup> by area	99 97	- -	1 3
Fe#2+	-	C2/c	<sup>§</sup> by area	98	-	2*

Footnotes: <sup>‡</sup>actual formulas were determined by Rietveld refinement imposing that M2 and T sites are occupied only by Li and Si, respectively, whereas the M1 site was constrained to be Al<sub>x</sub>Fe<sup>3+</sup><sub>1-x</sub> with 0 ≤ x ≤ 1; <sup>#</sup>weight and <sup>§</sup>area % of phases were determined by Rietveld refinement and by image analyses on back-scattered SEM pictures (see Figure 1), respectively; \*in this run-product the iron-rich phases is magnetite; \*the C2/c space group of pyroxene was determined by SAED-TEM data.

Table 4. Cell parameters obtained by powder X-ray and electron diffraction data

sample label	<sup>‡</sup> actual formula (a.p.f.u.)	<i>a</i> (Å)	* <i>a</i> (Å)	<i>b</i> (Å)	* <i>b</i> (Å)	<i>c</i> (Å)	* <i>c</i> (Å)	<i>β</i> (°)	* <i>β</i> (°)	<i>V</i> (Å <sup>3</sup> )	* <i>V</i> (Å <sup>3</sup> )
Fe#0	LiAlSi <sub>2</sub> O <sub>6</sub>	9.4657(1)	9.47(1)	8.3942(1)	8.39(1)	5.2204(1)	5.22(1)	110.15(1)	110.15(1)	389.41(1)	389.37(1)
Fe#20	Li(Al <sub>0.86</sub> Fe <sup>3+</sup> <sub>0.14</sub> )Si <sub>2</sub> O <sub>6</sub>	9.4898(1)	9.49(1)	8.4257(1)	8.43(1)	5.2317(1)	5.23(1)	110.14(1)	110.14(1)	392.74(1)	392.82(1)
Fe#40	Li(Al <sub>0.77</sub> Fe <sup>3+</sup> <sub>0.23</sub> )Si <sub>2</sub> O <sub>6</sub>	9.4992(1)	9.50(1)	8.4396(1)	8.44(1)	5.2362(1)	5.24(1)	110.128(1)	110.13(1)	394.15(1)	394.48(1)
Fe#50	Li(Al <sub>0.65</sub> Fe <sup>3+</sup> <sub>0.35</sub> )Si <sub>2</sub> O <sub>6</sub>	9.5306(1)	9.53(1)	8.4785(1)	8.48(1)	5.2488(1)	5.25(1)	110.136(1)	110.14(1)	398.20(1)	398.34(1)
Fe#60	Li(Al <sub>0.43</sub> Fe <sup>3+</sup> <sub>0.57</sub> )Si <sub>2</sub> O <sub>6</sub>	9.5598(1)	9.56(1)	8.5103(1)	8.51(1)	5.2588(1)	5.26(1)	110.177(1)	110.18(1)	401.59(1)	401.67(1)
Fe#80	Li(Al <sub>0.15</sub> Fe <sup>3+</sup> <sub>0.85</sub> )Si <sub>2</sub> O <sub>6</sub>	9.6127(2)	9.61(2)	8.5849(2)	8.58(2)	5.2778(1)	5.28(1)	110.178(1)	110.18(1)	408.81(2)	408.64(2)
Fe#100	LiFe <sup>3+</sup> Si <sub>2</sub> O <sub>6</sub>	9.6702(1)	9.67(1)	8.6626(1)	8.66(1)	5.2966(1)	5.30(1)	110.20(1)	110.20(1)	416.41(3)	416.54(1)
Fe#2+	-	9.6745(1)	9.67(1)	8.6757(1)	8.68(1)	5.2968(1)	5.30(1)	110.18(1)	110.18(1)	417.29(2)	417.56(1)

Footnotes: <sup>#</sup>the *C2/c* space group was used for the XRPD Rietveld refinements derived from SAED-TEM data; the Fe#2+ run-product was refined only by the Le Bail method; \*electron diffraction data.

sample label or study	actual formula (a.p.f.u.)	site	x	y	z	U <sub>iso</sub>
Fe#0	LiAlSi <sub>2</sub> O <sub>6</sub>	M2	0	0.276(1)	0.25	0.007(1)
		M1	0	0.907(1)	0.25	0.003(1)
		T	0.294(1)	0.093(1)	0.256(1)	0.004(1)
		O1	0.109(1)	0.083(1)	0.140(1)	0.003(1)
		O2	0.364(1)	0.267(1)	0.301(1)	0.006(1)
		O3	0.357(1)	0.987(1)	0.059(1)	0.005(1)
Fe#20	Li(Al <sub>0.86</sub> Fe <sup>3+</sup> <sub>0.14</sub> )Si <sub>2</sub> O <sub>6</sub>	M2	0	0.273(1)	0.25	0.002(1)
		M1	0	0.905(1)	0.25	0.002(1)
		T	0.294(1)	0.093(1)	0.258(1)	0.006(1)
		O1	0.110(1)	0.084(1)	0.141(1)	0.004(1)
		O2	0.364(1)	0.265(1)	0.304(1)	0.005(1)
		O3	0.355(1)	0.988(1)	0.058(1)	0.006(1)
Fe#40	Li(Al <sub>0.77</sub> Fe <sup>3+</sup> <sub>0.23</sub> )Si <sub>2</sub> O <sub>6</sub>	M2	0	0.271(1)	0.25	0.004(1)
		M1	0	0.905(1)	0.25	0.002(1)
		T	0.295(1)	0.092(1)	0.257(1)	0.004(1)
		O1	0.110(1)	0.084(1)	0.141(1)	0.003(1)
		O2	0.363(1)	0.265(1)	0.305(1)	0.004(1)
		O3	0.355(1)	0.989(1)	0.055(1)	0.006(1)
Fe#50	Li(Al <sub>0.65</sub> Fe <sup>3+</sup> <sub>0.35</sub> )Si <sub>2</sub> O <sub>6</sub>	M2	0	0.272(1)	0.25	0.001(1)
		M1	0	0.904(1)	0.25	0.001(1)
		T	0.295(1)	0.092(1)	0.258(1)	0.006(1)
		O1	0.111(1)	0.084(1)	0.144(1)	0.004(1)
		O2	0.364(1)	0.264(1)	0.309(1)	0.006(1)
		O3	0.356(1)	0.990(1)	0.056(1)	0.007(1)
Fe#60	Li(Al <sub>0.43</sub> Fe <sup>3+</sup> <sub>0.57</sub> )Si <sub>2</sub> O <sub>6</sub>	M2	0	0.266(1)	0.25	*0.004(1)
		M1	0	0.908(1)	0.25	
		T	0.295(1)	0.092(1)	0.259(1)	
		O1	0.112(1)	0.084(1)	0.144(1)	
		O2	0.364(1)	0.263(1)	0.311(1)	
		O3	0.355(1)	0.991(1)	0.054(1)	
Fe#80	Li(Al <sub>0.15</sub> Fe <sup>3+</sup> <sub>0.85</sub> )Si <sub>2</sub> O <sub>6</sub>	M2	0	0.268(1)	0.25	*0.004(1)
		M1	0	0.901(1)	0.25	
		T	0.295(1)	0.092(1)	0.262(1)	
		O1	0.113(1)	0.084(1)	0.147(1)	
		O2	0.367(1)	0.262(1)	0.319(1)	
		O3	0.354(1)	0.997(1)	0.054(1)	
Fe#100	LiFe <sup>3+</sup> Si <sub>2</sub> O <sub>6</sub>	M2	0	0.268(1)	0.25	*0.004(1)
		M1	0	0.899(1)	0.25	
		T	0.296(1)	0.089(1)	0.264(1)	
		O1	0.117(1)	0.083(1)	0.150(1)	
		O2	0.367(1)	0.264(1)	0.322(1)	
		O3	0.357(1)	0.999(1)	0.056(1)	

Footnote: \*refined with a unique global U<sub>iso</sub>. The average relative differences of atomic coordinates and U<sub>iso</sub> between single-crystal (Redhammer and Roth, 2004) and powder diffraction data (this study) for the LiAlSi<sub>2</sub>O<sub>6</sub> end-member are ~ 0.1 (max < 0.2) and ~ 0.3 (max < 0.9) %, respectively; the average relative differences of atomic coordinates and U<sub>iso</sub> between single-crystal (Redhammer and Roth, 2004) and powder diffraction data (this study) for the LiFe<sup>3+</sup>Si<sub>2</sub>O<sub>6</sub> end-member are ~ 0.2 (max < 0.6) and ~ 0.4 (max < 1.1) %, respectively.

Table 6. Cation-oxygen bond lengths.

sample label	actual formula (a.p.f.u.)	M2-O1	M2-O2	M2-O3	M2-O (average)	M1-O1	M1-O1	M1-O2	M1-O (average)	T-O1	T-O2	T-O3	T-O3	T-O (average)
Fe#0	LiAlSi <sub>2</sub> O <sub>6</sub>	2.108	2.280	2.241	2.210	1.943	1.995	1.831	1.923	1.648	1.580	1.622	1.630	1.620
Fe#20	Li(Al <sub>0.86</sub> Fe <sup>3+</sup> <sub>0.14</sub> )Si <sub>2</sub> O <sub>6</sub>	2.088	2.267	2.283	2.213	1.950	2.019	1.845	1.938	1.649	1.578	1.622	1.622	1.618
Fe#40	Li(Al <sub>0.77</sub> Fe <sup>3+</sup> <sub>0.23</sub> )Si <sub>2</sub> O <sub>6</sub>	2.075	2.266	2.315	2.218	1.956	2.022	1.854	1.944	1.651	1.579	1.619	1.621	1.617
Fe#50	Li(Al <sub>0.65</sub> Fe <sup>3+</sup> <sub>0.35</sub> )Si <sub>2</sub> O <sub>6</sub>	2.090	2.252	2.322	2.221	1.973	2.043	1.860	1.959	1.647	1.586	1.622	1.624	1.620
Fe#60	Li(Al <sub>0.43</sub> Fe <sup>3+</sup> <sub>0.57</sub> )Si <sub>2</sub> O <sub>6</sub>	2.067	2.237	2.376	2.226	1.979	2.031	1.892	1.967	1.645	1.587	1.616	1.632	1.620
Fe#80	Li(Al <sub>0.15</sub> Fe <sup>3+</sup> <sub>0.85</sub> )Si <sub>2</sub> O <sub>6</sub>	2.093	2.204	2.425	2.241	2.002	2.087	1.878	1.989	1.646	1.599	1.617	1.635	1.624
Fe#100	LiFe <sup>3+</sup> Si <sub>2</sub> O <sub>6</sub>	2.130	2.203	2.449	2.261	2.036	2.126	1.873	2.012	1.627	1.644	1.618	1.642	1.633

Figure 1

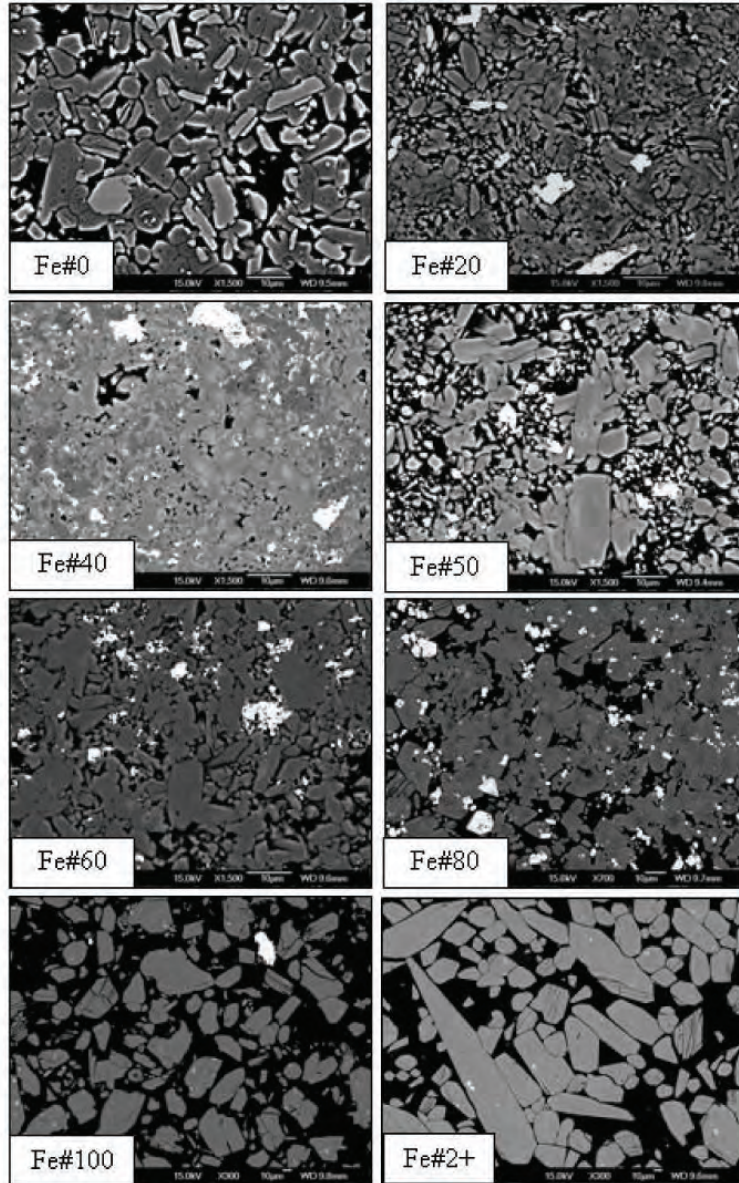
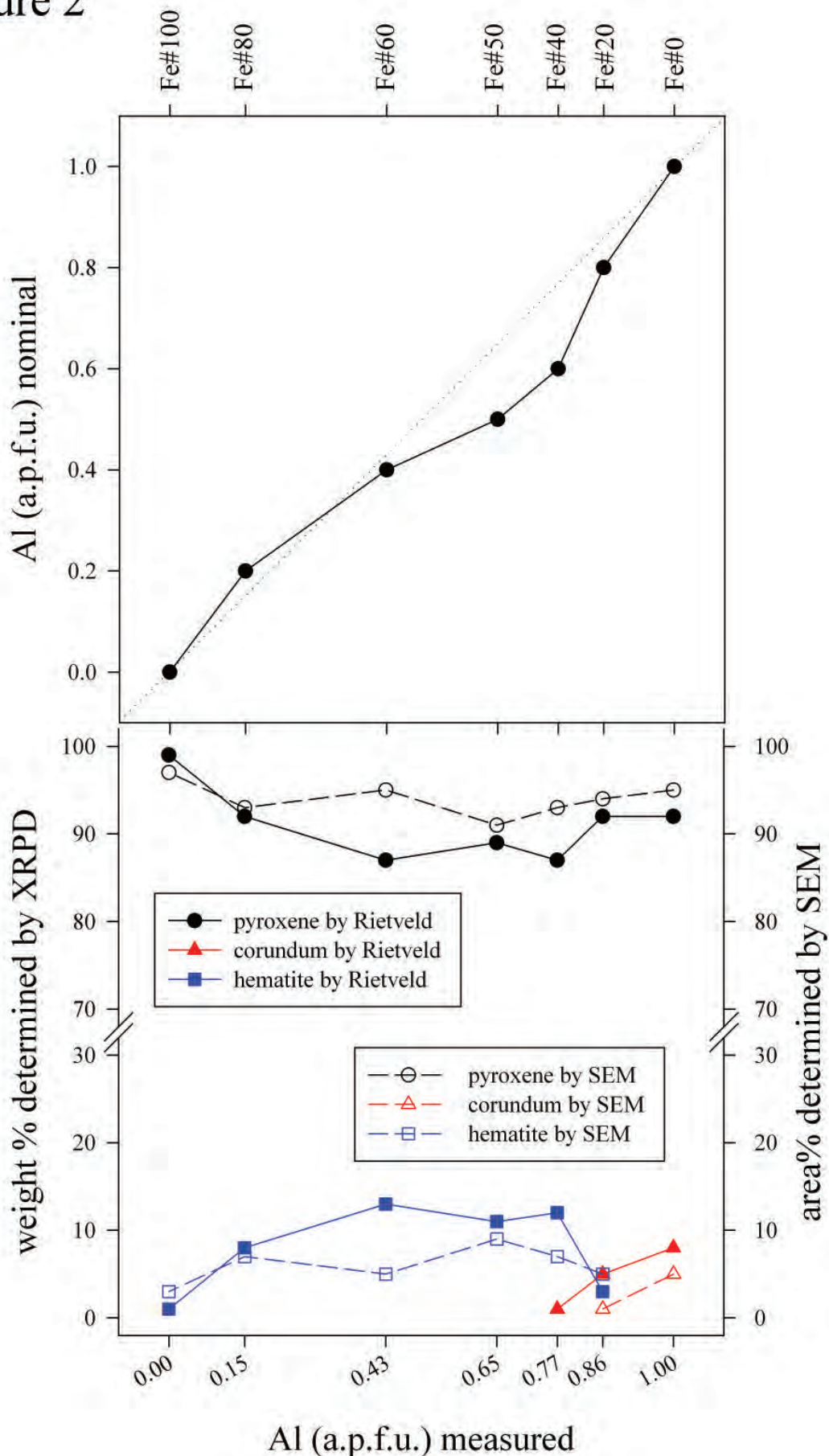


Figure 2





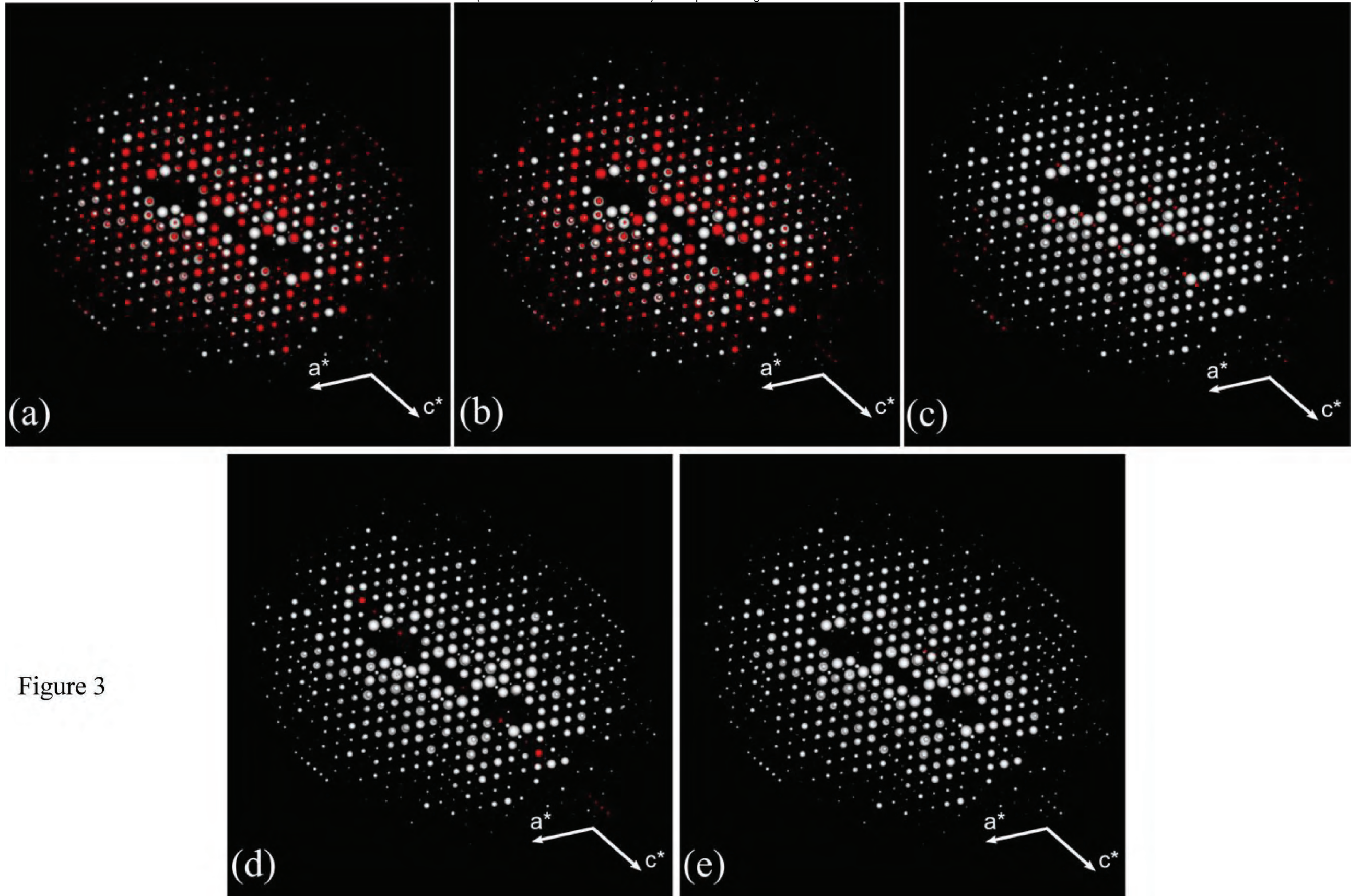


Figure 3



Figure 4

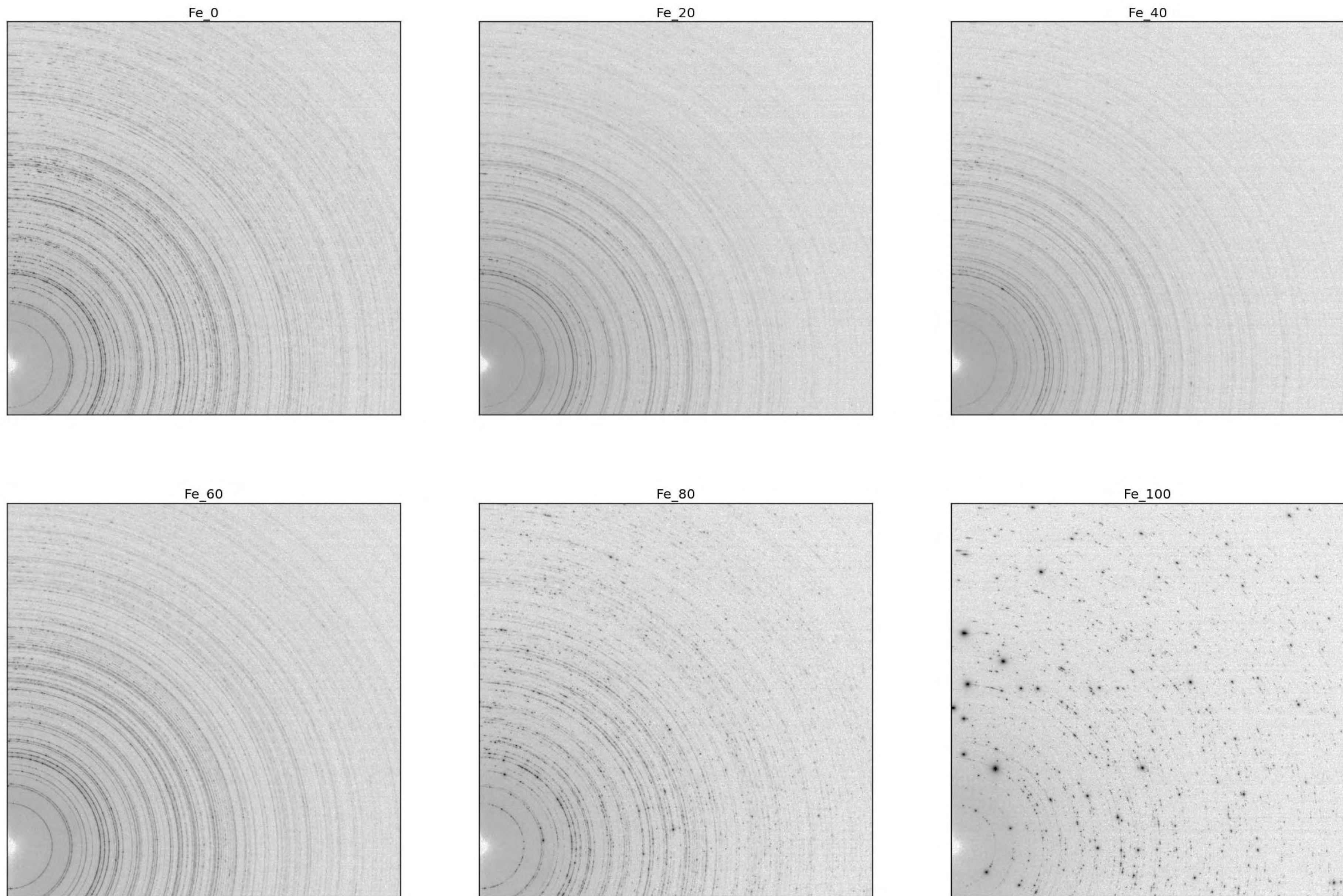




Figure 4S

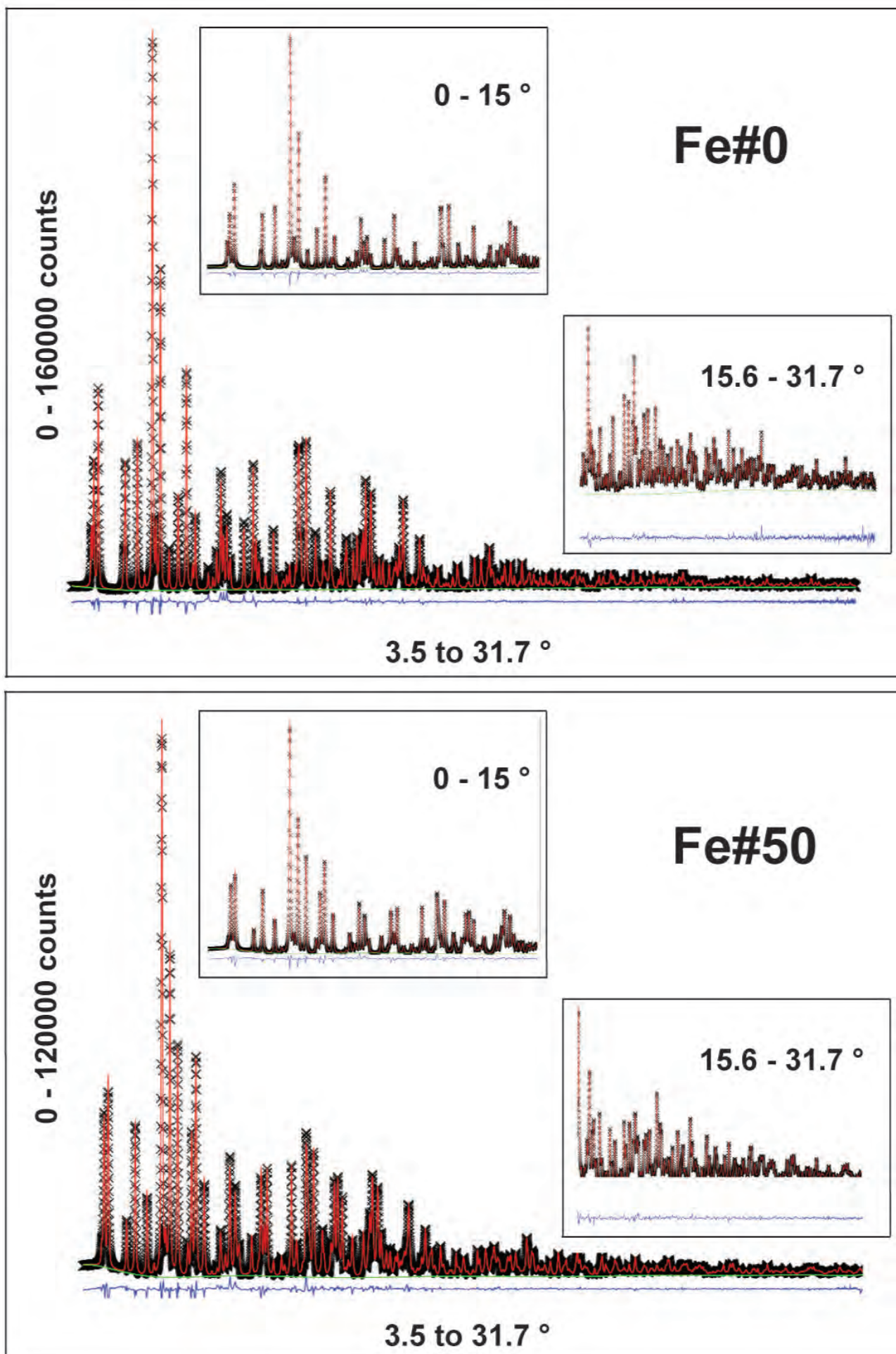


Figure 5

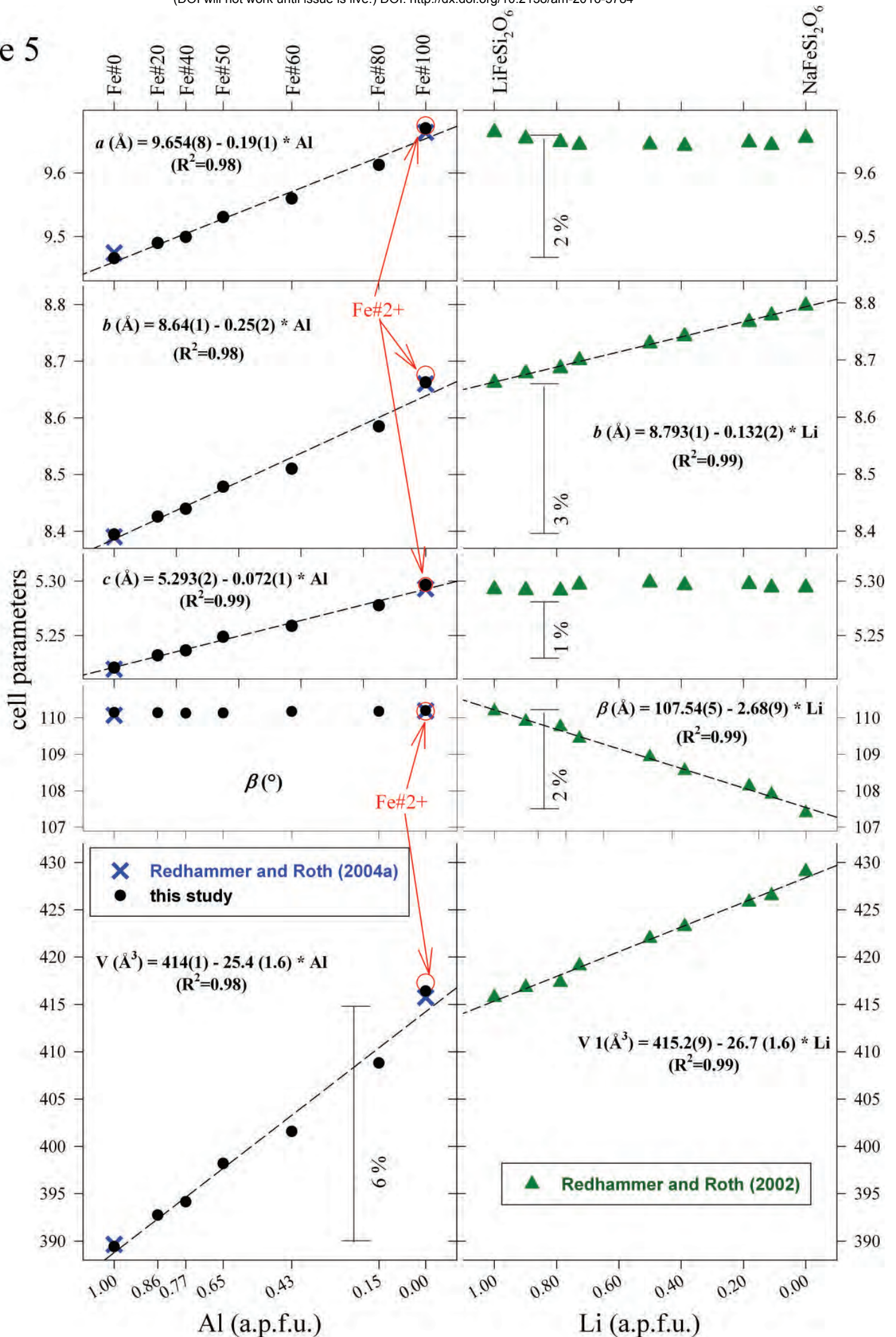




Figure 6

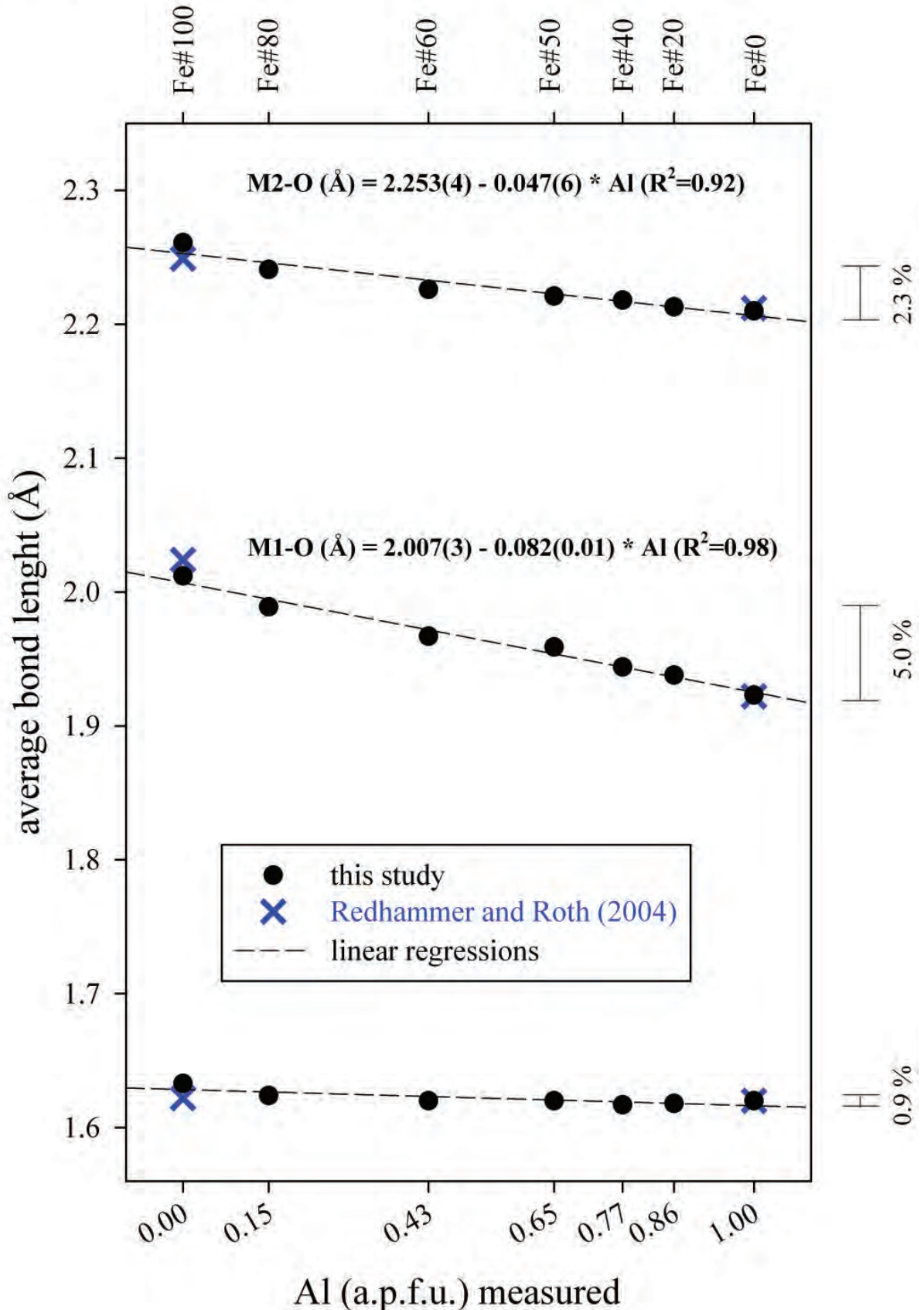


Figure 7

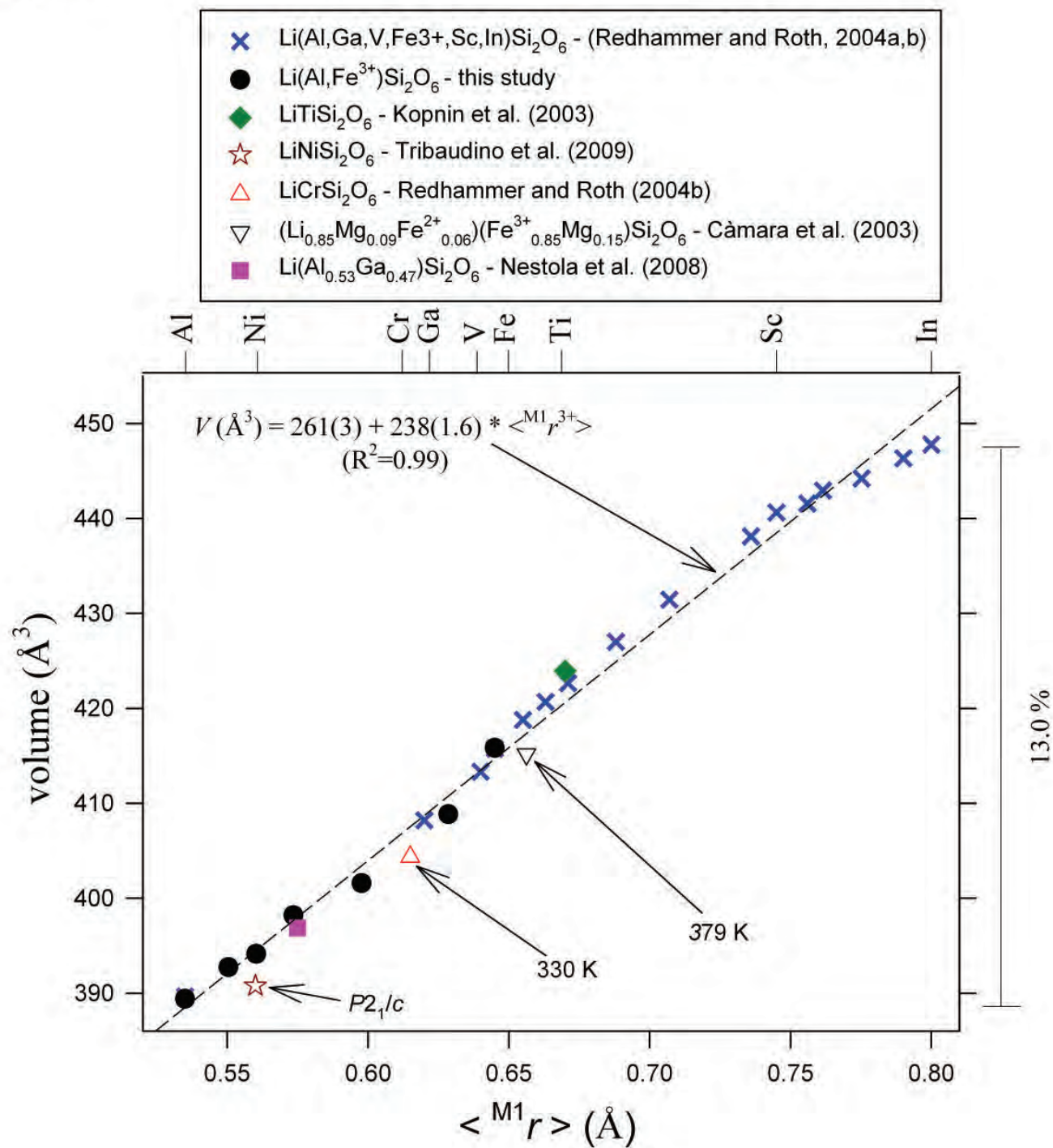


Figure 7S

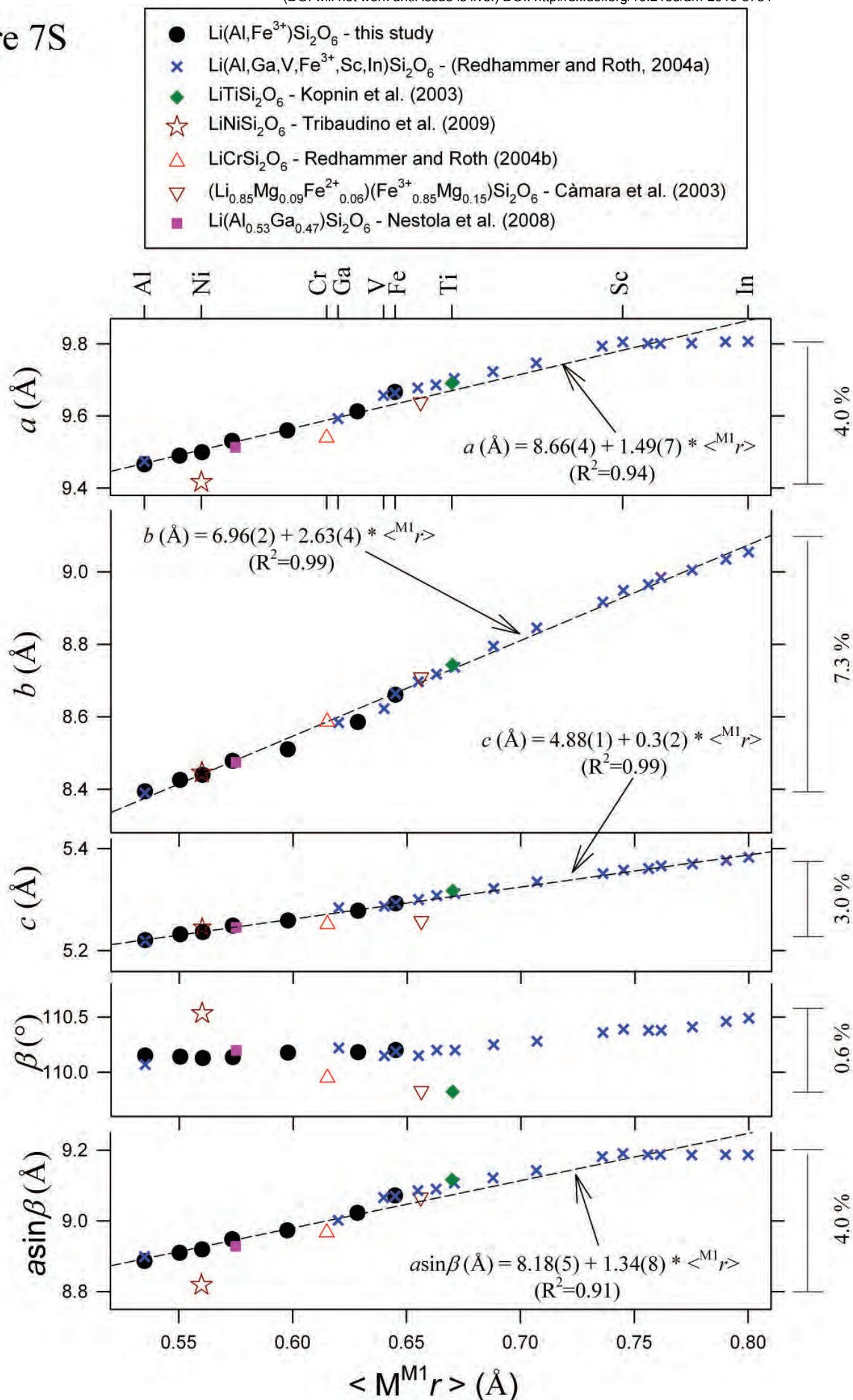




Figure 8

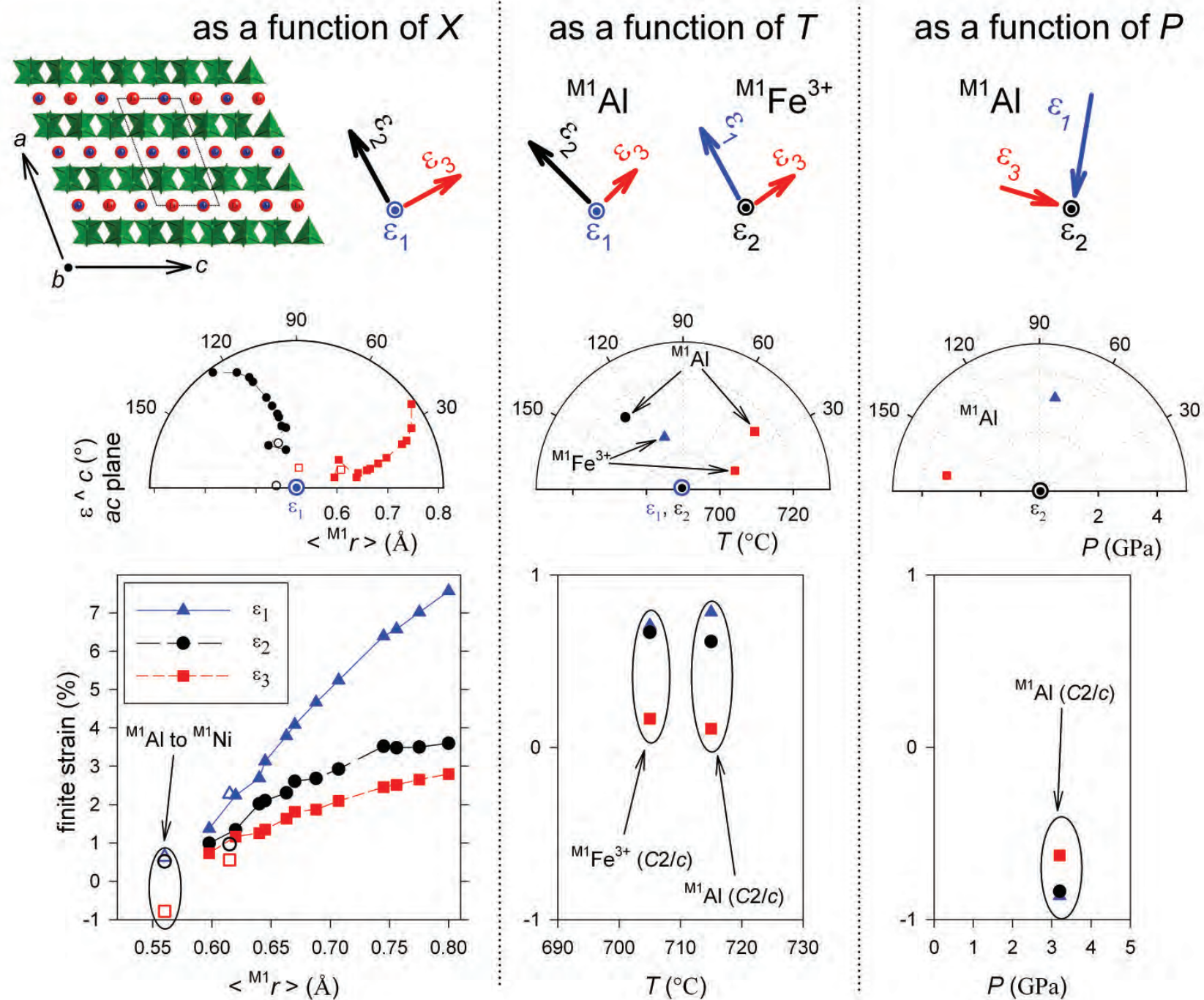
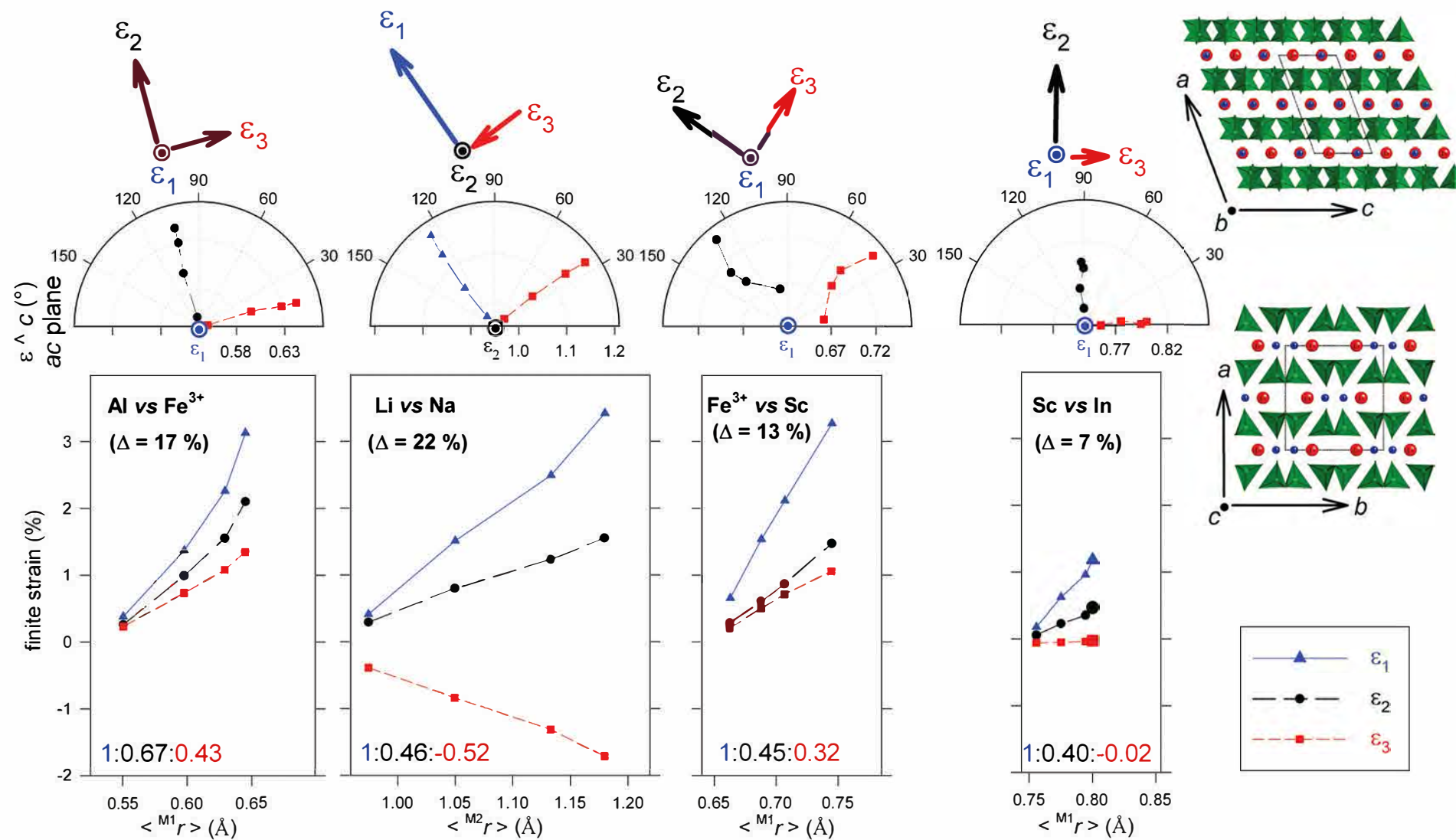
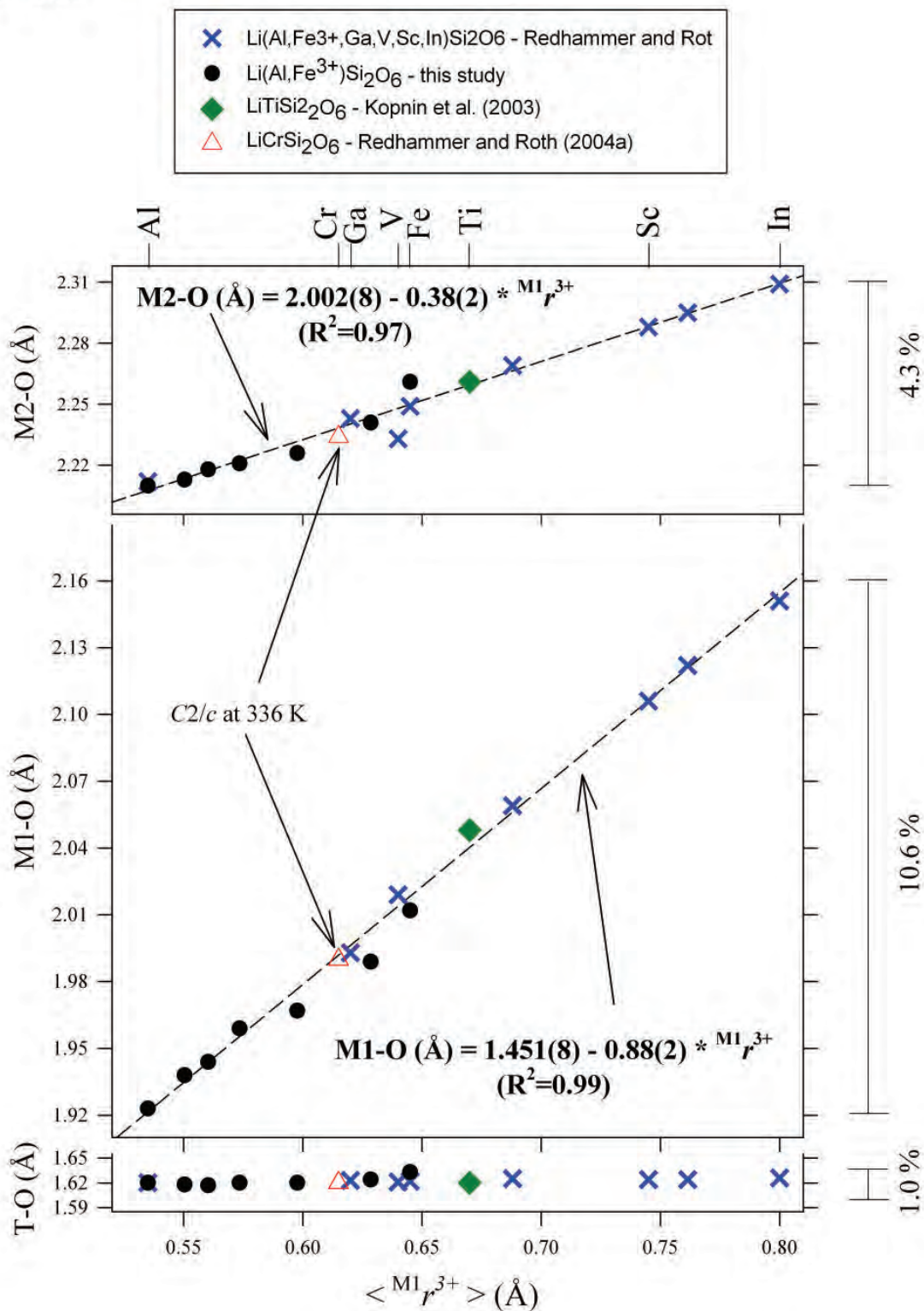


Figure 9



# Figure 10





# Figure 11

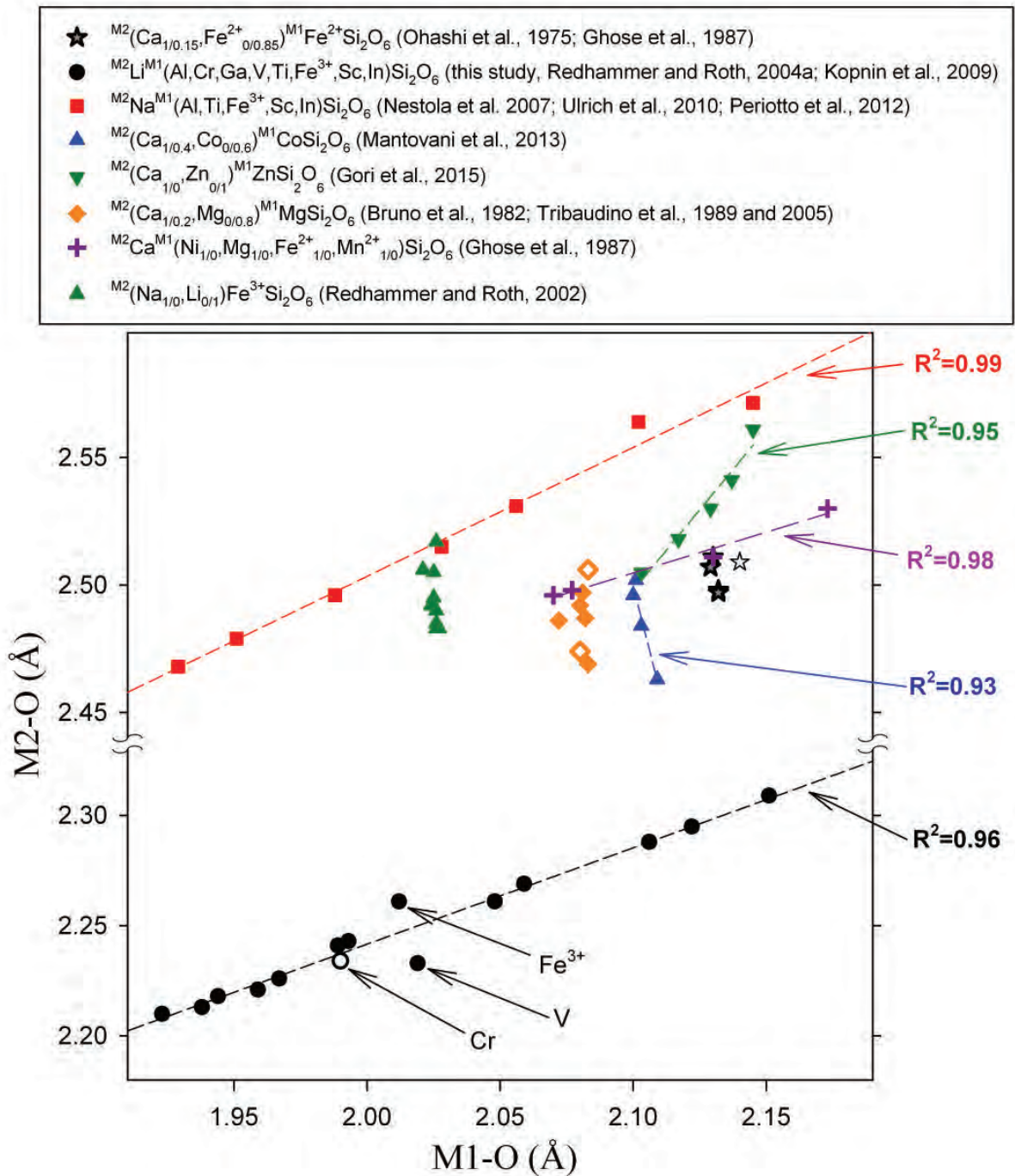


Figure 12

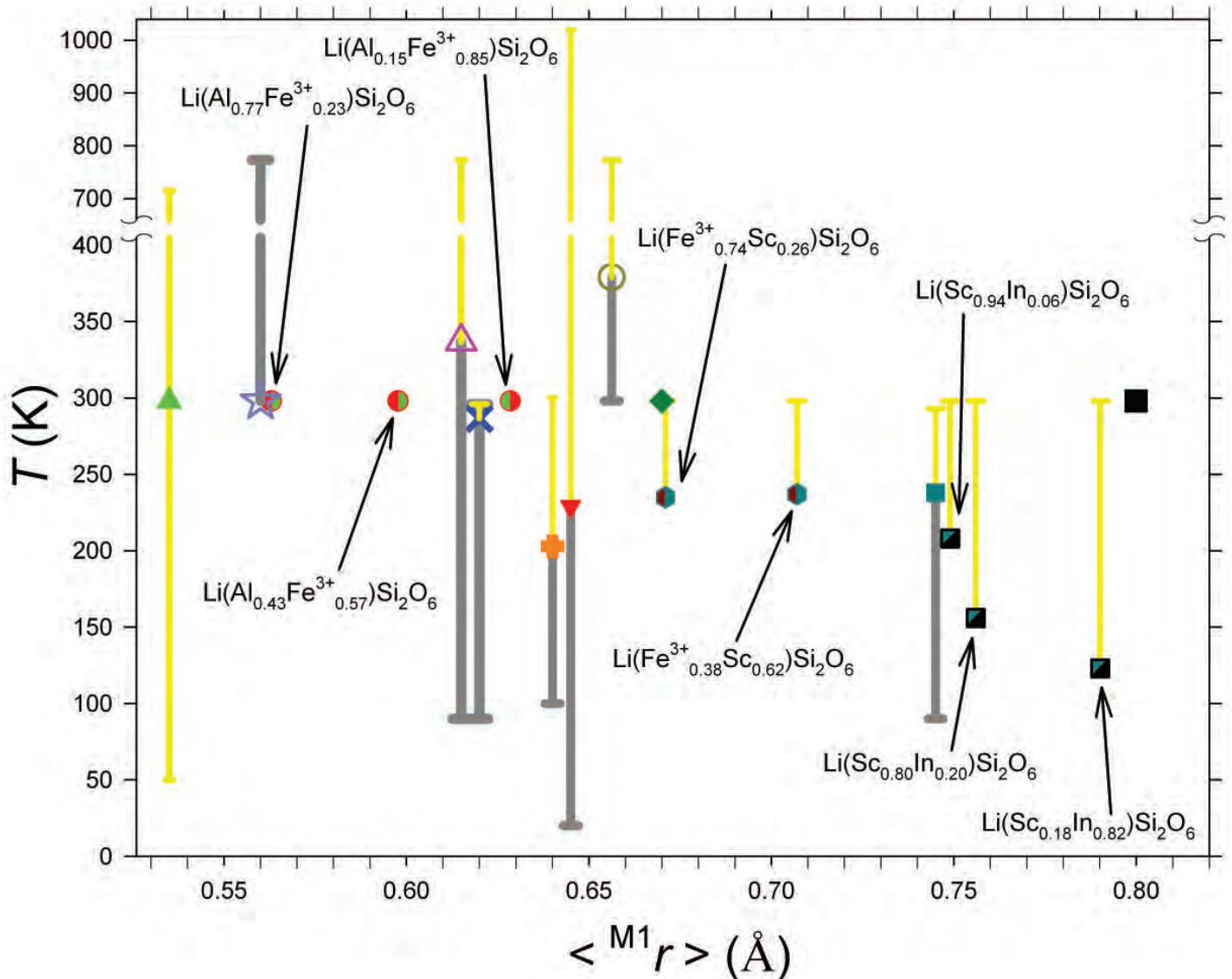
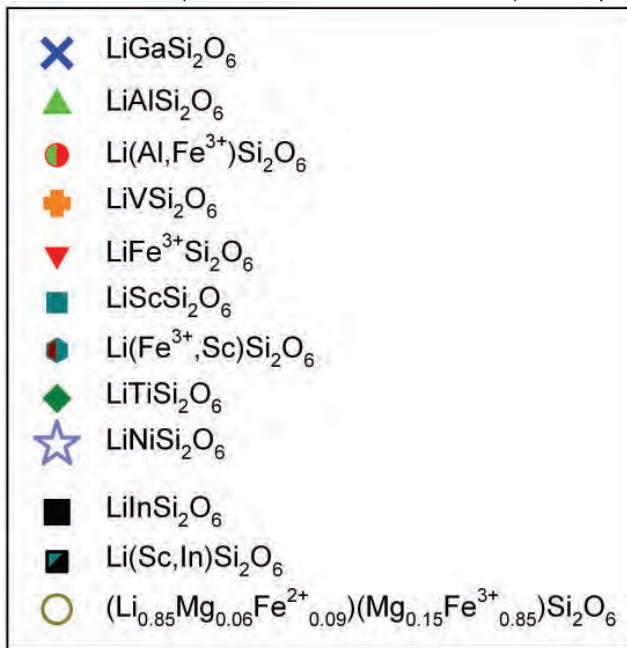




Figure 13

